國 立 交 通 大 學

電 信 工 程 學 系 碩 士 班

碩 士 論 文

多極化 MIMO 無線室內通道量測與建構

Measurement and modeling of Multi-polarized MIMO Channels in Indoor Environments

研究生 : 王至詰

指導教授 : 唐震寰 博士

中 華 民 國 九 十 五 年 七 月

多極化 MIMO 無線室內通道量測與建構

Measurement and modeling of Multi-polarized MIMO Channels in Indoor Environments

研 究 生：王至詰　　**Student : Zhi-Jie Wang**

指導教授：唐震寰　　**Advisor : Dr. Jenn-Hwan Tarng**

國 立 交 通 大 學

電 信 工 程 學 系 碩 士 班

碩 士 論 文

A Thesis
Submitted to Department of Communication Engineering
College of Electrical and Computer Engineering
National Chiao-Tung University
in Partial Fulfillment of the Requirements
for the Degree of
Master of Science
in
Communication Engineering
July 2005
Hsinchu, Taiwan, Republic of China

中 華 民 國 九 十 五 年 七 月

多極化 MIMO 無線室內通道量測與建構

研 究 生：王至詰　　指導教授：唐震寰博士

國 立 交 通 大 學

電信工程學系碩士班

摘要

通訊系統為了提高傳輸速率，因而在發射端與接收端使用了多單元天線架構，稱之為多輸入多輸出系統，其系統容量比傳統的一對一天線要來的高。本論文採用頻域向量通道響應系統量測從一對一到四對四的多輸入多輸出系統;並且在發射跟接收端使用多極化天線，於國立交通大學工程四館及電資中心內進行量測與分析。並且建構了多極化 MIMO 的通道模型經實驗驗證,適用性良好;而在通道響應量側，發現下列幾個現象:(1) 通道容量會隨陣列間距增加而增加,當其間距到 0.7 或 0.8 波長將會到達飽和而不再增加,非直接波的通道容量比直接波更容易看出間距的影響,原因為其多從路徑較多的關係;(2)多極化天線的使用,距離的增加跟非直視波的環境可以讓多極化的影響更明顯,並可讓間距的飽和長度縮短且獲得較高的通道容量;(3)通道頻率響應為隨機分布的情況,距離變化對其影響不大(4)環境內散射物的影響對通道容量有改善的效果

Measurement and modeling of Multi-polarized MIMO Channels in Indoor Environments

Student : Zhi-Jie Wang Advisor: Dr. Jenn-Hwan Tarng

Department of Communication Engineering
National Chiao Tung University

Abstract

Multiple-input-multiple-output (MIMO) systems have the potential to achieve very high capacities, The use of multiple antennas offers extended range and higher throughputs than conventional Single-input-single-output (SISO) systems. In this paper, we use multi-polarization antenna at both transmitter and receiver sides to analysis and measure channel response at 4th Engineering Building and MISRC. We also create a multi-polarized (MIMO) channel model validated by the measurement results. Some phenomena are observed from the measurement results and are summarized as the following: (1) It seems that the capacity increases as the elements spacing increases, which is due to the increase of de-correlation effect as the spacing increases. It is noted that this incremental saturates asymptotically when the array spacing is larger than 0.7 λ or 0.8 λ. It is found that the array spacing has not much effect on the capacity in LOS situation especially when the number of array element is small. However, when the number of array element is large and the total array length

is also large, the overall de-correlation effect due to array spacing is increased and the MIMO capacity is increased. The richness of multipath components in NLOS situations made all phenomena become more obvious. (2) It is found that polarization mismatch of array elements can increase the capacity. It is noted this effect may be enhanced by increasing the propagation distances. It is found that mismatch polarization can decrease the saturation length to 0.7 or 0.8 wavelengths. (3) The measurement results show that MIMO capacity frequency response is distributed randomly and changes slightly with propagation range. (4) The local scatterers around Tx/Rx array enhance MIMO capacity.

誌謝

在碩士的研究生涯，我一度因為身體不適，中斷學業，但是唐震寰老師並未因此放棄對我指導，而讓我有機會能完成在無線通訊領域的研究，在此我對老師致上最衷心的感謝，並感謝實驗室中的學弟妹跟女友曉妍能給我精神上的鼓勵，以及實驗量測中的協助,最後感謝我的家人對我的關懷跟支持，讓我在求學過程中能有所依靠

僅以此篇論文獻給所有關心我的人

王至詰

國立交通大學，新竹市

中華民國九十五年七月

Contents

List of Figures

List of Tables

Chapter 1

Introduction

In recent years the application of antenna arrays for wireless cellular system has received much attention, as they improve the coverage and quality of such system by combating interference and fading. It has also been shown that by exploiting antenna arrays at both the transmitters and receivers, Multiple-Input Multiple-Output (MIMO) communications systems using multi-antenna arrays simultaneously during transmission and reception have generated significant interest. Multiple antenna technologies are being considered as a viable solution for the next generation of mobile and wireless local area networks (WLAN). The use of multiple antennas offers extended range, improved reliability and higher throughputs than conventional single antenna communication systems. MIMO systems also have emerged as one of the most promising approaches for high-data rate wireless systems, MIMO communication architecture which employs multiple antennas at both the transmitter and the receiver, has recently emerged as a new paradigm of extremely spectrum-efficient wireless communications in rich multipath environment. MIMO

wireless systems have been shown theoretically to have significantly higher capacity than more traditional single-input multiple-output (SIMO) systems. Large capacity is obtained via the potential decorrelation between the channel coefficient of the multiple-input/multiple-output (MIMO) radio channel, since a fully correlated MIMO radio channel only offers one subchannel, while a completely decorrelated radio channel potentially offers multiple subchannels depending on the antenna configuration and propagation effects. Increase in the correlation coefficient results in capacity decrease and, finally, when the correlation coefficient equals to unity, no advantage is provided by the MIMO architecture.

The channel capacity can be increased in a sufficiently rich scattering environment by using MIMO arrays at both the transmit side and receive side. It has been demonstrated in [1] that the so-called MIMO channel can be considered as a system of number of parallel spatial subchannels allowing the transmission of parallel symbol data streams.

Analysis and design of multielement antenna systems in mobile fading channels requires a model for space-time cross correlation among the links of the MIMO channel. There are numerous applications of the proposed correlation model in multielement antenna systems with space-time modems to calculating MIMO channel capacity [2]-[10], such as the joint selection of antenna spacing and interleaving depth

[11], channel interpolation using the wiener filter [12]. Considering effect number of array elements;Winters [13] showed that the theoretical capacity of an (M,M)array is much larger than for a single channel, since M independent channels established with each channel having about the same maxium data rate as a single channel. The effect of antenna spacing is reported in reference [14] that the antenna spacing has little effect on capacity when the antenna spacing exceeds 0.5 wavelength, However, our measurement results and the result shown in reference [14] found that the antenna spacing actually affects significantly. In the reference [15], it show that when the antenna array spacing exceed 0.5wavelength , the capacity will increase very slowly, but according to our research , we find that when antenna array spacing exceed one wavelength，capacity will saturation，but between 0.1 wavelength to the 1 wavelength , the capacity will linearly increase when antenna array spacing increase. In most of the paper, the antenna array spacing is equal, but we find that the unequally array spacing maybe obtains the greater capacity than the equal array, in the reference [15], we can observe the same result.

Considering including multipolarized array effect, depolarization mechanisms caused by scatterers and antenna design result in gain imbalance and correlation between channel matrix elements. a limited number of physical models [16]-[18], [19],[20] have addressed the polarization multiplexing/diversity issue, mainly because the

(de)coupling effect between orthogonal polarization is a complex mechanism. Most existing physical models are only valid for unipolarized Rayleigh channel have recently shown that the capacity does not vary significantly with range, although other channel characteristic, such as the delay spread, **K**-factor, and cross-polar discrimination are affected, sometimes significantly. the usual base transceiver station **(BTS)** antennas in Broad-band wireless access **(BWA)** systems have relatively narrow bandwidths in the vertical direction (typically 6°),the scattering mechanisms in **BWA** macrocellular networks can be considered as mostly 2-D processes [21],[22],[23]-[27]. Note that the assumption of 2-D propagation is the basis of a large number of recent models of **MIMO** channels [21],[22], [23]-[27].

It seems that not many papers focused on the effects of vector fields (multipolarized fields), bandwidth and carrier frequency on MIMO channel capacity, which may have practical uses such as in UWB radio systems. In this thesis, effects of propagation, array polarizations, array spacing, number of array elements, bandwidth, and carrier frequency on UWB-MIMO capacity are explored with extensive indoor measurements. To further investigate the insight mechanisms, we have proposed a physical MIMO radio channel model, which is based on the spatio-temporal elliptical model. The model includes effect of polarization mismatching between the incident field and the received antenna, and is validated by the measurement results.

This thesis is composed of 6 chapters: In chapter 2, we introduce the fundamental Theory of UWB-MIMO channels and Spatio-Temporal channel Elliptical Model. In order to obtain the channel characteristics, measurement set-up and sites was elucidated in chapter 3. In chapter 4, the effects of number of array element, array spacing, propagation, array multi-polarization, and bandwidth on UWB-MIMO channel capacity are explored by indoor measurements. In chapter 5, extension of a stochastic geometry-based scattering model to analysis and design of multielement antenna systems in mobile fading channels including characteristics of (MIMO) multipolarized transmission. A brief conclusion is provided in chapter 6.

Chapter 2

Fundamental Theory of UWB-MIMO Channels and Spatio-Temporal channel Elliptical Model

2.1 MIMO Channel Model

A scheme of (M_T,N_R) antenna array is shown in Fig2.1. Each antenna can transmit symbols originating from a different modulation scheme and carrys an independent data stream.

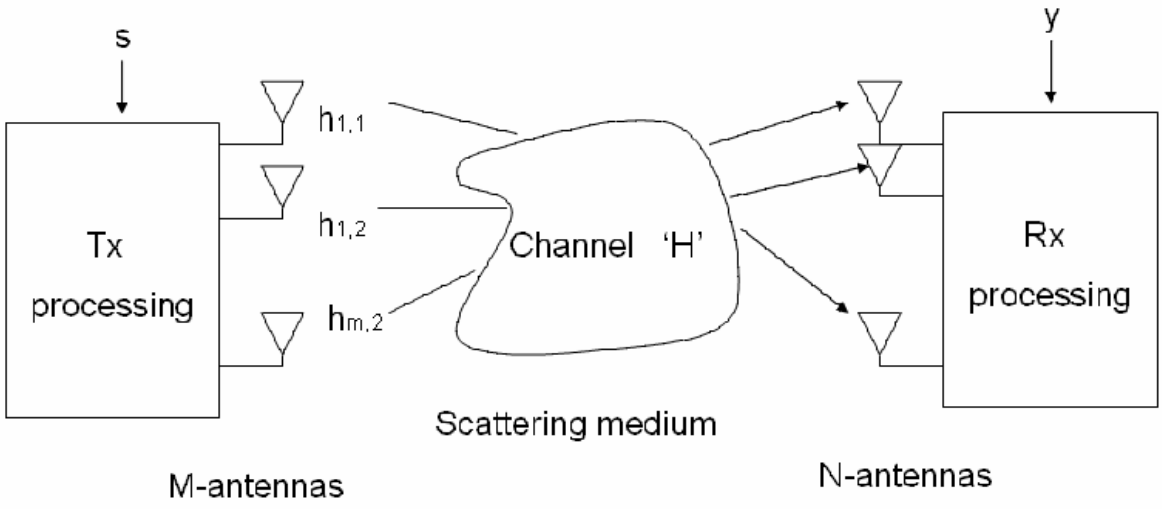

Fig. 2.1 MxN MIMO channel representation, where M=m and N=n represent number of antennas at Tx and Rx, respectively.

The baseband input-output relationship is given by

$$y(\tau) = H(\tau) \times s(\tau) + n(\tau) \qquad (2\text{-}1)$$

where $s(\tau)$ is the transmitted signal, $y(\tau)$ is the receiver signal, $n(\tau)$ is AWGN (Additive White Gaussian Noise) and $\times$ denotes convolution. Each element of the channel impulse response matrix $H(\tau)$ is the impulse response from a transmit antenna to a receiver antenna.

The MIMO channel without noise and with representation of the channel matrix *H* can be expressed as:

$$\mathbf{H}(\tau) = \sum_{l=1}^{L} H_l \delta(\tau - \tau_l) \qquad (2\text{-}2)$$

where *L* is the number of taps (time bins) of the channel model, *H*(τ) is the *MxN* matrix of the channel impulse responses. $\mathbf{H}(\tau) \in C^{MXN}$ and is given by

$$\mathbf{H} = \begin{bmatrix} H_{11} & H_{12} & . & . & . & H_{1n} \\ H_{21} & H_{22} & & & & . \\ . & . & & & & . \\ H_{m1} & . & & & & H_{mn} \end{bmatrix} \qquad (2\text{-}3)$$

Before explaining model structure, some knowledge of different classifications in the area of channel modeling is introduced.

Wideband Models vs. *Narrowband Models*: the MIMO channel models can be divided into the wideband models and the narrowband models directly by considering the bandwidth of the system. The wideband models treat the propagation channel as frequency selective, which means that different frequency subchannels have different

channel response. On the other hand, the narrowband models assume that the channel has frequency non-selective fading and therefore the channel has the same response over the entire system bandwidth.

Field Measurements vs. *Scatter Models*: to model the MIMO channel, one approach is to measure the MIMO channel responses through field measurements. Some important characteristics of the MIMO channel can be obtained by investigating the recorded data and the MIMO channel model can be modelled to have similar characteristics. Models based on MIMO channel measurements were reported in [4]. An alternative approach is to postulate a model (usually involving distributed scatters) that attempts to capture the channel characteristics. Such a model can often illustrate the essential characteristics of the MIMO channel as long as the constructed scattering environment is reasonable. It is the environment of scatters that is in detail studied here.

Non-physical Models vs. *Physical Models*: the MIMO channel models can be divided into the non-physical and physical models. The non-physical models describe MIMO channel via statistical characteristics obtained from the measured data. Another category is the physical models that are based on parameter setup and theoretical results. In general, these models choose some crucial physical parameters to describe the MIMO propagation channels. Some typical parameters include Angel of Arrival

(AoA), Angle of Departure (AoD), carrier frequency, antenna spacing.

2.2 MIMO Channel Capacity

When the transmitted power is equally allocated to each transmit element and frequency subchannel, the UWB-MIMO channel capacity can be expressed as [28] and [29]

$$C = \frac{1}{W}\int_{W} \log_2 \det\left(I_{n_R} + \frac{\rho}{n_T} H(f) H^*(f) \right) df \qquad \text{bits/s/Hz} \qquad (2\text{-}4)$$

where n_T and n_R are the numbers of Tx and Rx antenna array elements, respectively, and W is the overall bandwidth of the MIMO channel, $H(f)$ is the normalized frequency response matrix of each narrow-band subchannel, * is the complex conjugate, and ρ is the average SNR at each receiver branch over the entire bandwidth. Since the measured UWB-MIMO matrices include the pathloss, we had to do a normalization to set the average receiver SNR to a specific value. Here, we normalize the frequency response of every narrow-band subchannel using a common factor such that

$$\int_{W} E\left(\left\| H(f) \right\|_F^2 \right) df = W n_T n_R \qquad (2\text{-}5)$$

We also write capacity formula (2-4) into another form [12]

$$C_i = \frac{1}{N_f} \sum_{f}^{N_f} \log_2 \left(\det\left(I_{n_R} + \frac{\rho}{n_T} H_i(f) H_i^*(f) \right) \right) \qquad \text{bits/s/Hz} \qquad (2\text{-}6)$$

where N_f is frequency components.

The normalisation factor for each UWB measurement snapshot T_i (*i* is the time or snapshot index) was calculated separately. This removed the effect of large-scale spatial fading, which can be significant for dynamic measurements, and ensured that only the small-scale: spatial fading was observed. T_i has dimensions of $n_R \times n_T \times N_f$, where n_R, n_T, N_f are the number of receive antennas, transmit antennas and frequency components respectively. Each 4x4 measured channel snapshot had dimensions of $(4 \times 4 \times 801)$, thus providing a sufficient number of independent samples for normalisation. The normalized UWB channel H_i is given by

$$H_i = \frac{T_i}{\hat{\eta}_k}, \text{ and} \tag{2-7}$$

where $\hat{\eta}_k$ is the normalisation factor estimate and is given by

$$\hat{\eta}_k^{\,2} = \frac{1}{n_R n_T N_f} \sum_{f=1}^{N_f} \sum_{j=1}^{n_R} \sum_{k=1}^{n_T} \left| T_{i,f,j,k} \right|^2, \tag{2-8}$$

The goal of channel normalisation is usually to scale the channel response so that the expectation of its power is unity. We refer to this as *unity-gain* normalization.

2.3 The Geometrically Based Single Bounce Elliptical Model

The Geometrically Based Single Bounce Elliptical Model (**GBSBEM**) is used to simulate power-delay-angle profiles, power delay profiles, joint time-angle statistics,

marginal characteristics of the Direction-of-Arrival, and narrowband fading envelopes. The **GBSBEM** appropriate surrounded by clutter, and scatterers are distributed between and around both the transmitter and receiver. Let us consider a multipath component which arrives at time τ_i. the multipath component is the result of a single reflection/scattering (a single bounce path), then the scatterer causing the reflection/scattering must lie on an ellipse with major axis half length *a*, and minor axis half length b, as shown in Figure 2-1, The quantities *a* , *b*, and *f* are given by

$$F = d_0/2 \qquad (2\text{-}9)$$

$$a = c\tau_i/2 \qquad (2\text{-}10)$$

$$b = \sqrt{a^2 - f^2} \qquad (2\text{-}11)$$

The scatterer resulting in a single bounce multipath component arriving at time τ_i lies at coordinates (X_s,Y_s) such X_s and Y_s satisfy

$$\frac{X_s^2}{a^2} + \frac{Y_s^2}{b^2} = 1 \qquad (2\text{-}12)$$

This is because the distance from the scatterer at (X_s,Y_s) to the transmitter at (-*f*, 0), and the distance from the scatterer to the receiver at (f,0), sum to $2a = c\tau_i$ provided that the scatterer lies on the ellipse (*a*, *b*). It is assumed that scatteres are uniformly distributed in space. All of the scatterers giving rise to single bounce multipath components arriving between time τ and $\tau + \Delta\tau$ lie in the region bounded on the inner edge by an ellipse with parameters

$$a_1 = c\tau/2 \qquad (2\text{-}13)$$

$$b_1 = \sqrt{a_1^2 - f^2} \qquad (2\text{-}14)$$

and on the outer edge by the ellipse with parameters

$$a_2 = c(\tau + \Delta\tau)/2 \qquad (2\text{-}15)$$

$$b_2 = \sqrt{a_2^2 - f^2} \qquad (2\text{-}16)$$

The region bounde by these two ellipse is illustrated in Figure 2-2. The area of this region is

$$A = \pi(a_2 b_{2d} - a_1 b_1) \qquad (2\text{-}17)$$

The probability density function (pdf) for the x and y coordinates of scatterers, giving rise to single bounce multipath components arriving between times τ and $\tau + \Delta\tau$

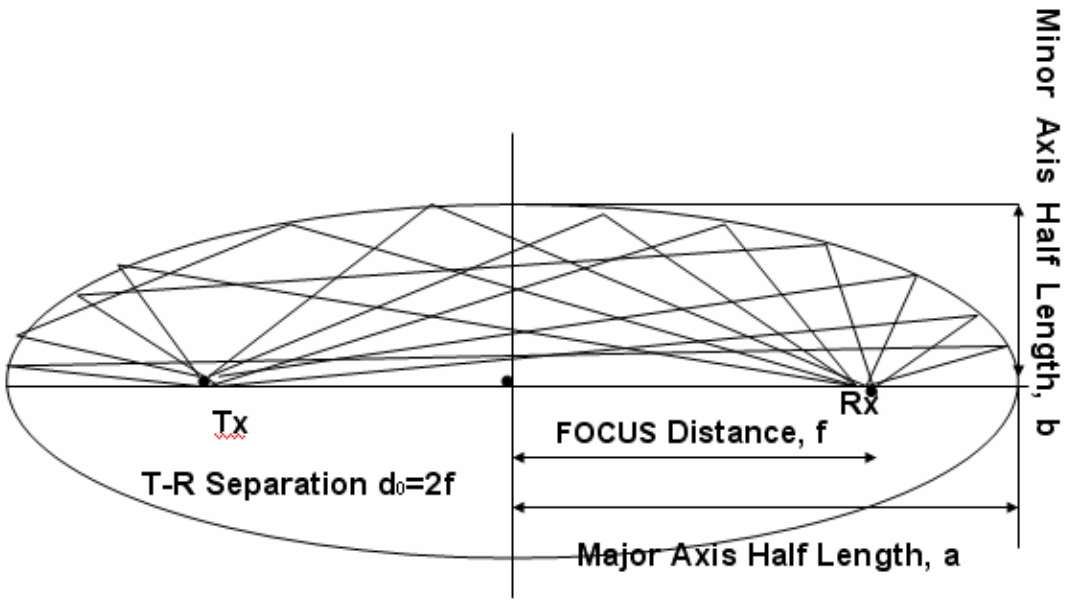

Fig.2-1 the locus of all points where a scatterer must lie ,which results in a single bounce multipath component with delay τ_i is an ellipse.

is given by

$$f_{xy}(x,y) = \frac{1}{A} = \frac{1}{\pi(a_2 b_2 - a_1 b_1)}, \qquad x,y \in \{ \frac{x^2}{a_1^2} + \frac{y^2}{b_1^2} \geq 1, \frac{x^2}{a_1^2} + \frac{y^2}{b_1^2} \leq 1 \} \quad (2\text{-}18)$$

To determine the cumlative distribution (cdf) for the **DOA** conditioned on the **TOA,** We first find the probability that a single bounce multipath component arrives with a Direction-Of-Arrival, Φ_i between 0 and an angle Φ, at time τ_i prior to τ. The time τ determines an ellipse given by parameters $\{a, b\}$ from (2-10) and (2-11). To find this cdf, we first compute the area of the region in the ellipse $\{a, b\}$ for which $0 \leq \Phi \leq \Phi$, where Φ is measured clockwise from a line drawn between the transmitter and receiver as shown in Figure 2-3. This area is

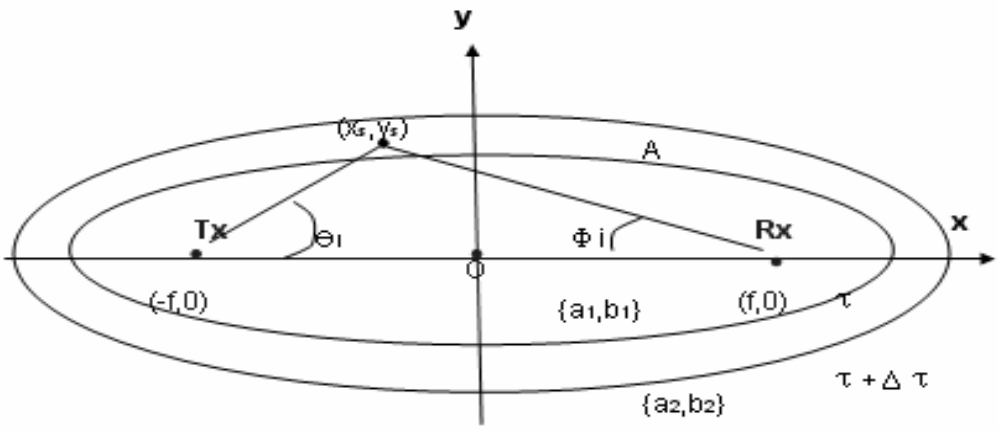

Fig. 2-2 Geometry for determining the statistics of Direction-Of-arrival (DOA), Φ_i, given that a multipath component arrives at time τ_i, $\tau \leq \tau_i \leq \tau + \Delta\tau$.

$$R_{a,b}(\Phi) = \int_{-a}^{a\left(\frac{f-a\cos\Phi}{a-\cos\Phi}\right)} b\sqrt{1-\left(\frac{x}{a}\right)^2}\,dx + \frac{(f-x_\Phi)y_\Phi}{2}$$

$$= -\frac{ab}{2}\left(\cos^{-1}\left(\left(\frac{f-a\cos\Phi}{a-f\cos\Phi}\right)-\pi-\frac{(f-a\cos\Phi)b\sin\Phi}{(a-f\sin\Phi)^2}\right)+\frac{b^4\sin\Phi\cos\Phi}{2(a-f\cos\Phi)^2}\right.$$

$$= -\frac{ab}{2}\left(\cos^{-1}\left(\left(\frac{f-a\cos\Phi}{a-f\cos\Phi}\right)-\pi\right)+\frac{b^4\sin\Phi\cos\Phi}{2(a-f\cos\Phi)^2}\right. \qquad (2\text{-}19)$$

Thus, the probability that a single bounce multipath component, arriving with a Time-Of-Arrival τ_i, such that $\tau \le \tau_i \le \tau + \Delta\tau$, has a Direction-Of-Arrival between 0 and Φ is given by

$$\Pr(0 \le \Phi_i < \Phi \mid 0 \le \Phi_i \le \pi,\ \tau \le \tau_i \le \tau + \Delta\tau) = \frac{R_{a_2,b_2}(\Phi) - R_{a_1,b_1}(\Phi)}{A/2} \qquad (2\text{-}20)$$

Through symmetry, we may deduce that for $-\pi \le \Phi_i < 0$,

$$\Pr(-\pi \le \Phi_i < \Phi \mid -\pi \le \Phi_i \le 0,\ \tau \le \tau_i \le \tau + \Delta\tau)$$

$$= \frac{A/2 - (R_{a_2,b_2}(-\Phi) - R_{a_1,b_1}(-\Phi))}{A/2} \qquad (2\text{-}21)$$

Then for $-\pi \le \Phi_i \le \pi$ we obtain the following cumulative distribution function (cdf) for Φ

$$\mathbf{X}_\Phi = a\left(\frac{f-a\cos\Phi}{a-f\cos\Phi}\right), \qquad \mathbf{Y}_\Phi = \frac{b^2\sin\Phi}{a-f\cos\Phi}$$

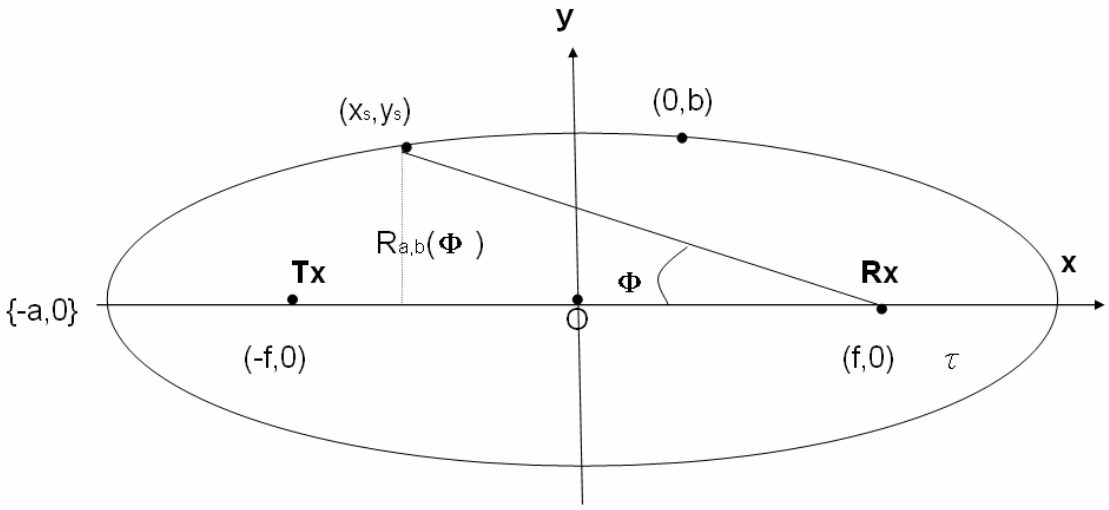

Fig. 2-3 The region of the ellipse {a,b} swept out by Φ

$$F_{\Phi|\tau d}(\Phi \mid \tau \le \tau_i \le \tau + \Delta\tau) = \Pr(-\pi \le \Phi_i < \Phi \mid -\pi \le \Phi_i \le 0,\ \tau \le \tau_i \le \tau + \Delta\tau)$$

$$= \begin{cases} \frac{1}{2} - \frac{R_{a_2,b_2}(-\Phi) - R_{a_1,b_1}(-\Phi)}{A} & \cdots\cdots -\pi \le \Phi \le 0 \\ \frac{1}{2} + \frac{R_{a_2,b_2}(\Phi) - R_{a_1,b_1}(\Phi)}{A} & \cdots\cdots 0 \le \Phi < \pi \end{cases} \qquad (2\text{-}22)$$

Our goal is to determine the distribution of the Direction-Of-Arrival, Φ_i, for a particular multipath component as a function of Time-Of-Arrival. In order to simplify notation, it is convenient to introduce the normalized multipath delay $r_i = c\tau_i/d_0 = \tau_i/\tau_0$. To obtain the cdf for Φ_i conditioned on the normalized multipath delay, r_i, we take the limit of (2-18) as $\Delta\tau$ goes to zero which gives:

$$F_{\Phi|r}(\Phi|r_i) = \begin{cases} \frac{1}{2\pi}\cos^{-1}\left(\frac{1 - r_i\cos\Phi}{r_i - \cos\Phi}\right) - \frac{\sqrt{r_i^2 - 1}\sin(-\Phi)(1 - r_i\cos\Phi)}{2\pi(2r_i^2 - 1)(r_1 - \cos\Phi)^2} & \cdots\cdots -\pi \le \Phi \le 0 \\ 1 - \frac{1}{2\pi}\cos^{-1}\left(\frac{1 - r_i\cos\Phi}{r_i - \cos\Phi}\right) + \frac{\sqrt{r_i^2 - 1}\sin(\Phi)(1 - r_i\cos\Phi)}{2\pi(2r_i^2 - 1)(r_i - \cos\Phi)^2} & \cdots\cdots 0 \le \Phi < \pi \end{cases} \qquad (2\text{-}23)$$

The conditional pdf for the DOA, Φ_i, may be found by differentiating (2-23) with

respect to Φ. This gives

$$f_{\Phi|r}(\Phi|r_i) = \frac{(r_i^2 - 1)^{3/2}(r_i^2 - 2r_i\cos\Phi + 1)}{\pi(2r_i^2 - 1)(r_i - \cos\Phi)^3} \qquad -\pi \le \Phi \le \pi \quad (2\text{-}24)$$

Chapter 3

Measurement Set-up and Sites

Due to reflection, refraction and scattering of radio waves insides a building, the transmitted signal most often reaches the receiver by more than one path. In order to characterize the performance of MIMO systems in real environments, the objectives of this chapter is to describe the measurement set-up and the measurement campaign and extracts the parameters from measurement raw data. For improving the link quality or to increase the system capacity for future indoor wireless communications, multipolarized UWB antenna can be designed and implemented efficiently by obtaining the channel characteristics in different environments, the **UWB-MIMO** channel measurement methods are proposed for analyzing each composition of multipath response. We classify propagation scenarios as following:

Scenario I: Line-of-Sight (LOS) with local scatterers;

Scenario II: Line-of-Sight (LOS) without local scatterers;

Scenario III: Non-Line-of-Sight (NLOS) with local scatterers; and

ScenarioIV: Non-Line-of-Sight (NLOS) without local scatterers.

3.1 Measurement System and Setup

In order to obtain the channel characteristics, the wideband channel measurement is performed to analyze the MPCs. A typical frequency domain channel sounder is shown in Fig. 3-1. A vector network analyzer contains a synthesized frequency sweeper and an S-parameter test set. At port 1 the S-parameter test set transmits a known signal level for each frequency step and detects the received complex response of the channel, S_{21} (f), at port 2.

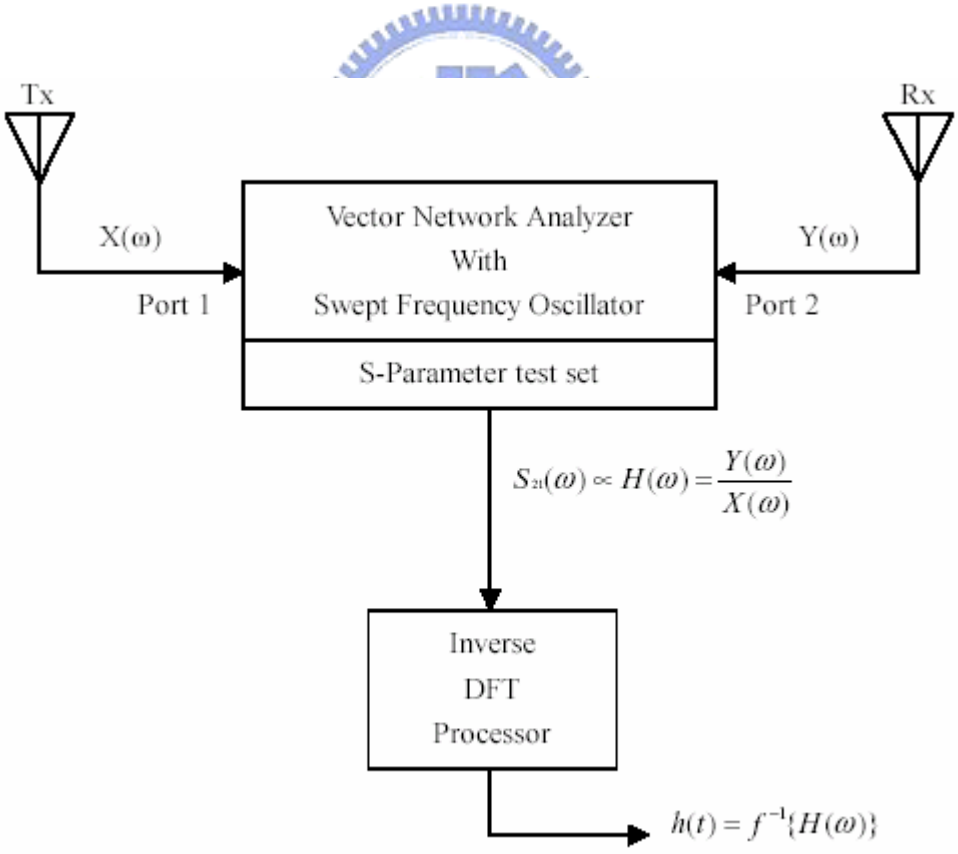

Fig. 3-1 Frequency domain channel response measurement system.

The Agilent 8719ET vector network analyzer is exploited to measure the channel

response between two ends and the measurement system diagram is shown in Fig. 3-2. Besides the network analyzer, the frequency domain channel sounding system contains one pair omni-directional antennas operating range from 5.1-5.8 GHz with antenna gain is 2.5dBi, long low loss cables. The photograph of the physical system is

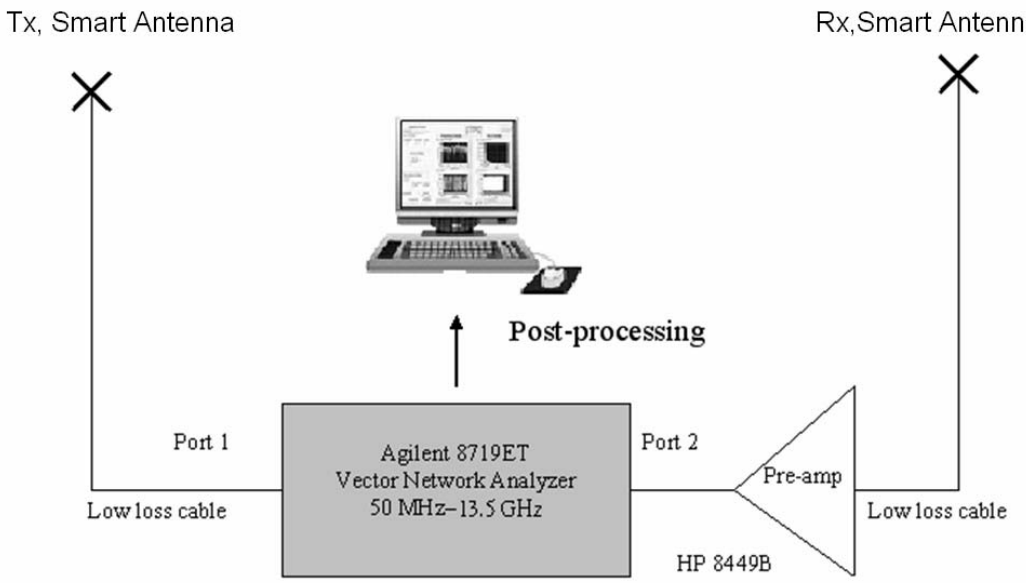

Fig. 3-2 measurement system diagram

shown in Fig. 3-3. Figure 3-4 illustrates the picture of one the antenna. Vertical and horizontal patterns of the transmitted and received antennas are shown in Fig. 3-5. The signal from the receiving antenna is through a preamplifier (with a gain of 30dB) via an internal application and the swept frequency band is from 5.2-5.7GHz (0.5GHz of frequency span). With 0.625MHz steps corresponding to 801points, we would be

able to detect multipath with a time delay up to 1600ns. Besides the network analyzer, the time-domain channel response can be obtained by taking the inverse Fourier transform (IFFT) of the frequency-domain channel response. Table 3.1 lists the main parameters in the measurement.

Fig. 3-3 A photo of the frequency domain channel sounding system

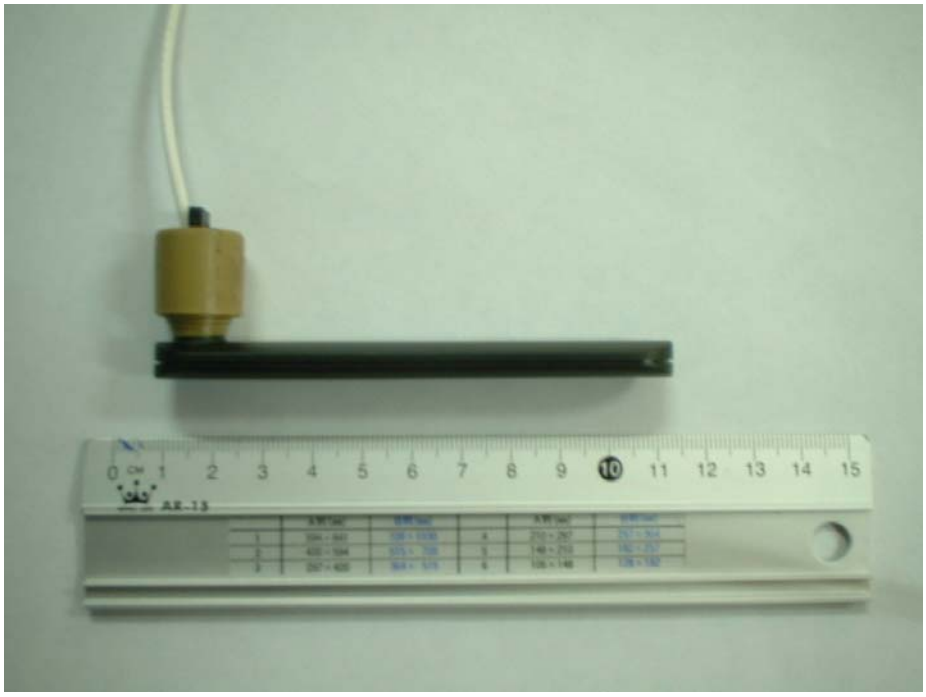

Fig. 3-4 A photo of the antenna provided by SmartAnt

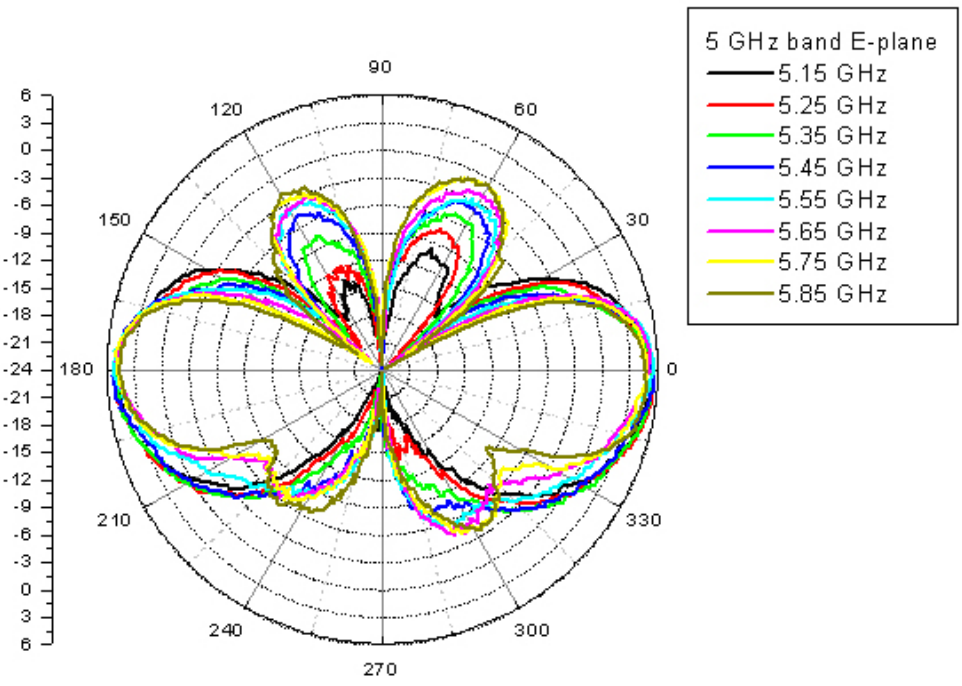

(a)

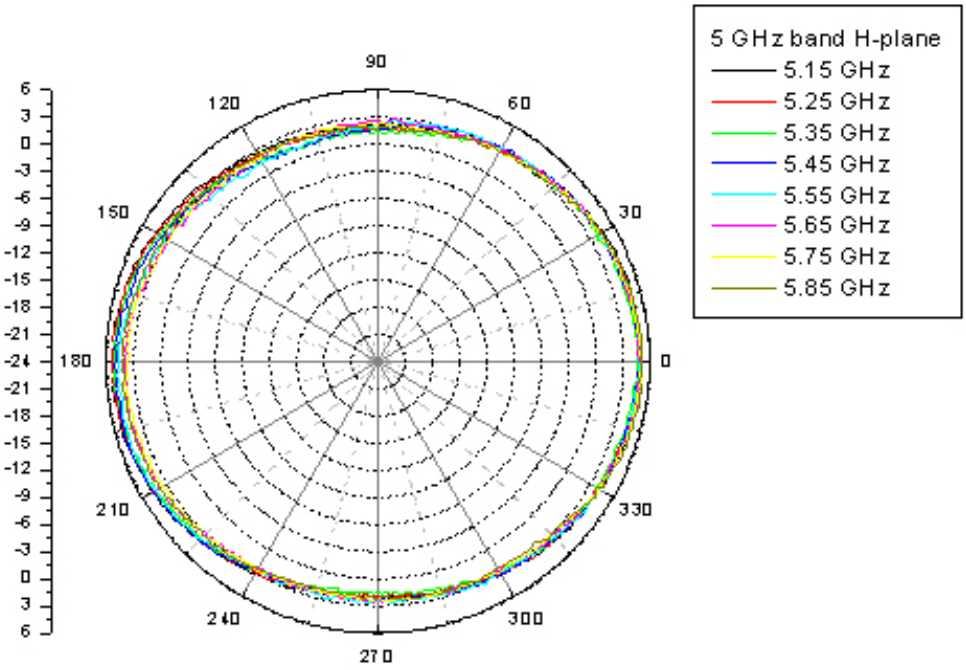

Fig. 3-5 (a) Vertical; and (b) Horizontal patterns of the transmitted and received antennas provided by SmartAnt

Table 3.1 : List of set-up parameters of the measurement system

Parameter	**Value**
Frequency band	5.2 GHz to 5.7 GHz
Bandwidth (frequency span)	0.5 GHz
Number of points over the band	801
Transmitted power	10 dBm
Preamplifier gain	30 dB
Antenna gain	2.5 dBi

In order to investigate effects of carrier frequency and bandwidth, a pair of UWB antennas are also employed for the measurement from 3GHz to5 GHz. Here, the array spacing is also explored to see the spacing effect on element correlation, i.e., channel capacity.

Because our measurement system is just an SISO system with 2 omni directional antennas at both ends, we have simulated the mxn MIMO channels by moving the Tx and Rx to the ULA (Uniform Linear Array) fixed points, where m or n = 2-4. We have performed the measurement when the environment varies very slowly with time. During the measurement, the Rx and Tx antennas are at a height of 1.0 m and 1.5 m , respectively, above the ground.

It is noted that the polarization of Tx and Rx antennas may be vertical or horizontal. They can be different. The following table shows the polarization arrangements of Tx and Rx antenna for the measurement campaign.

Table 3.2 Polarization Arrangement (PA) of the mxn MIMO system

Polarization Arrangement No.	4x4 MIMO	4x3 MIMO	3x3 MIMO	3x2 MIMO	2x2 MIMO	2x1 MIMO	1x1 SISO
1	VHVH x VHVH	VHVH x VHV	VHV x VHV	VHV x VH	VH x VH	VH x V	V x V
2	VHVH x VVVV	VHVH x VVV	VHV x VVV	VHV x VV	VH x VV	VH x V	V x V
3	VHVH x HHHH	VHVH x HHH	VHV x HHH	VHV x HH	VH x HH	VH x H	V x V
4	VVVV x VHVH	VVVV x VHVH	VVV x VHV	VVV x VH	VV x VH	VV x V	V x V
5	HHHH x VHVH	HHHH x VHVH	HHH x VHV	HHH x VH	HH x VH	HH x V	H x V
6	VVVV x VVVV	VVVV x VVV	VVV x VVV	VVV x VV	VV x VV	VV x V	V x V
7	HHHH x HHHH	HHHH x HHH	HHH x HHH	HHH x HH	HH x HH	HH x H	H x H

(V: vertical polarization , H: horizontal polarization)

3.2 Measurement Environment

The measurement was performed at 3rd (sites A and B) and 9th floors (site C) of Engineering Buliding no.4, and at 1st (sites D and E) and 8th floors (site F), of the Microelectronics and Information System Research Center (MISRC) in the National Chiao-Tung University, Hsinchu, Taiwan. The floor layouts of these sites are shown in Fig. 3-6. In order to analyze how the local scatterer affects the capacity, the measurements are carried at site B (NLOS with local scatterers) site C (LOS with local scatterers), site D (LOS without local scatter), and site E (NLOS without local scatterers). Table 3-3 illustrates Tx-Rx distance for each measurement.

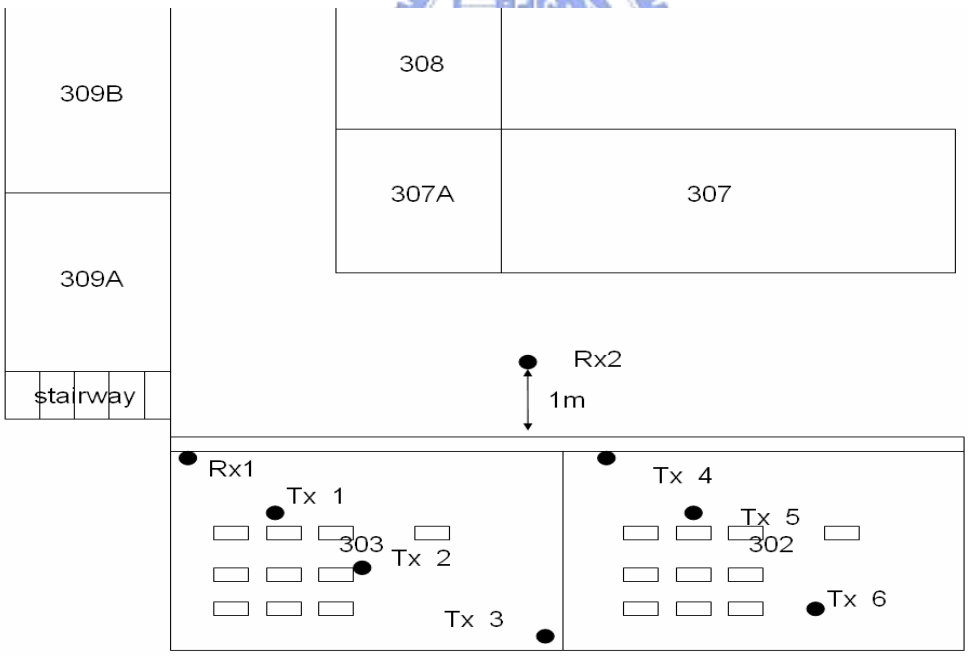

Fig 3-6 (a) Floor layout of Sites A (LOS, Rx1-Tx1-Tx4), and B (NLOS, Rx2-Tx4-Tx6), which are mainly located at 303 and 302 classrooms, respectively, of Engineering Building No.4.

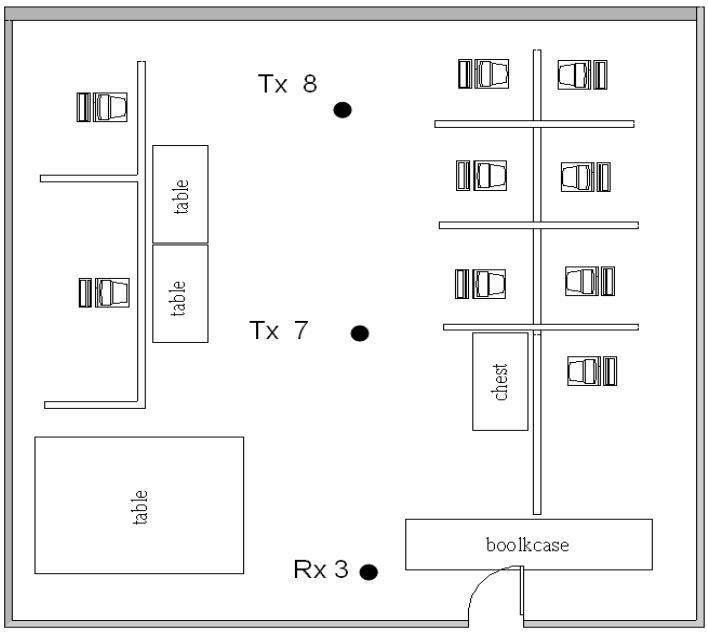

Fig 3-6 (b) Floor layout of Site C (NLOS with local scatterers , Rx3-Tx7-Tx8) which is located at Lab 901 of the 4th Engineering Building;

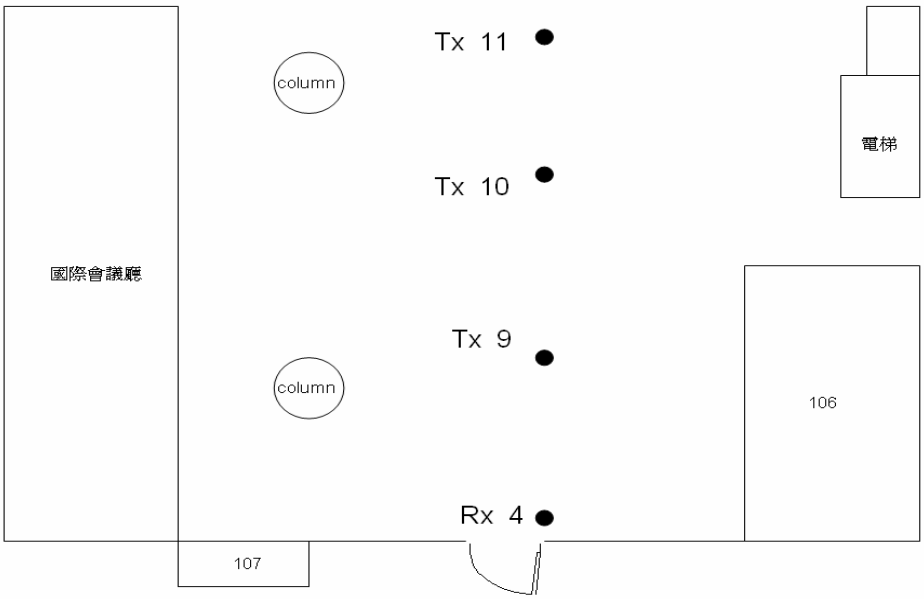

Fig. 3-6 (c) Floor layout of Site D (LOS with local scatterers Rx4-Tx9-Tx10-Tx11) which is located at 1st floor of MISRC;

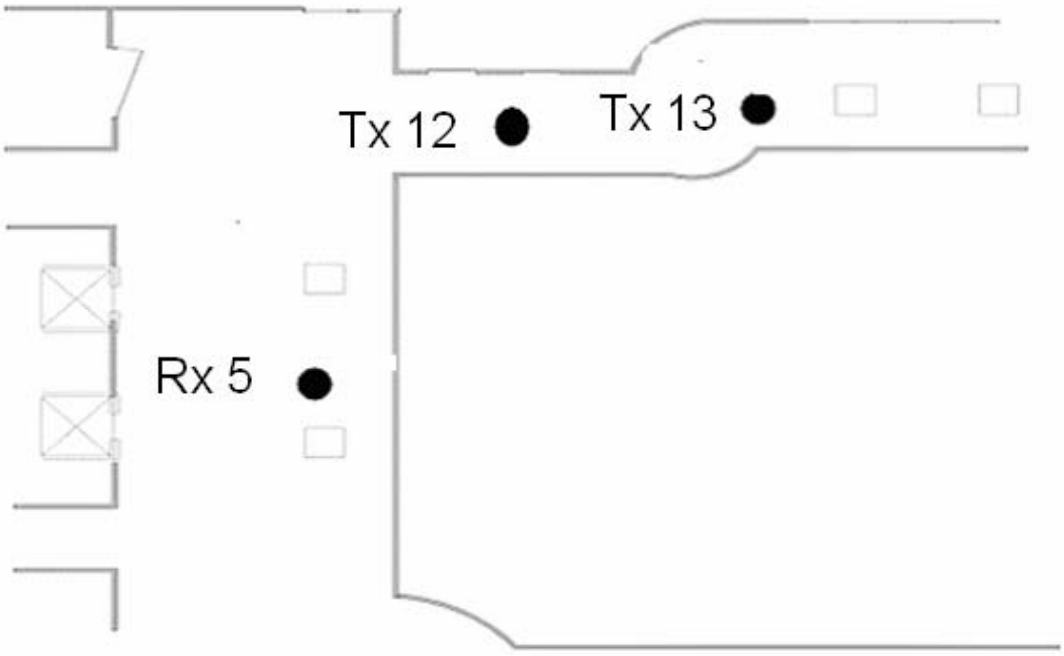

Fig 3-6 (d) Floor layout of Site E (NLOS without local scatterer Rx5-Tx12-Tx13) which is located at 1st floor of MISRC;

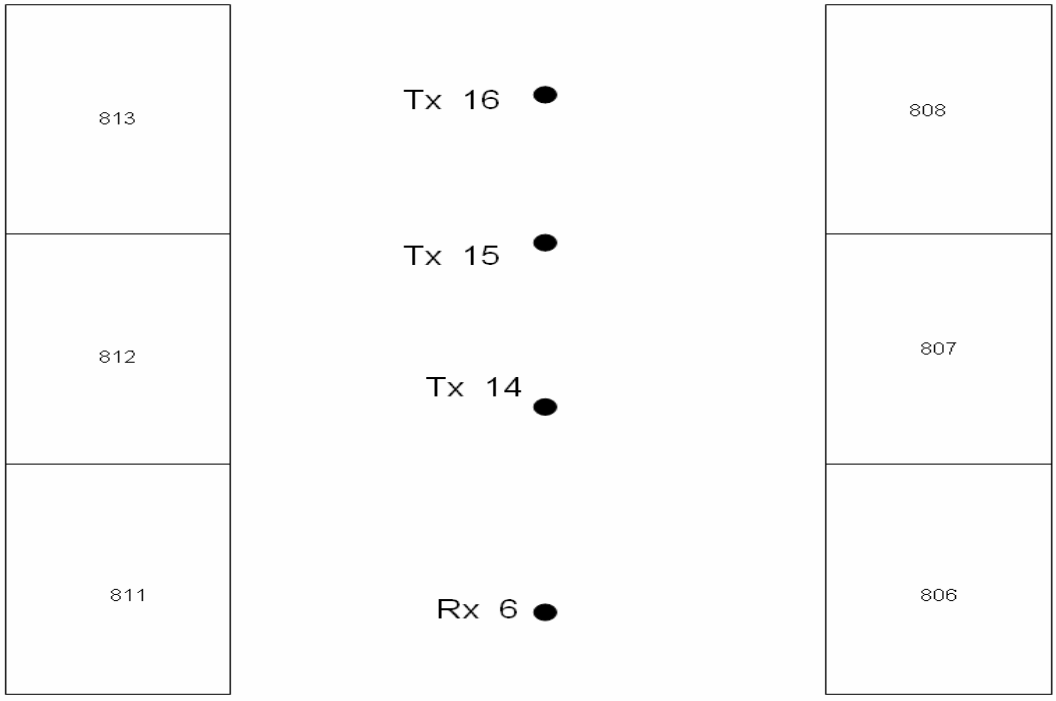

Fig 3-6 (e) Floor layout of Site F (LOS without local scatterers Rx5 –Tx14 -Tx15-Tx16), which is located at 8th floor of MISRC;

Table 3-3 Propagation distance between Rx-Tx at each measurement site.

Site No.	Propagation Distance (Tx-Rx)
Site A	Tx1-Rx1 =4m; Tx2-Rx1 =7m; Tx3-Rx1 =14m
Site B	Tx4-Rx2 =4m;Tx5-Rx2 =7m; Tx6-Rx2 =14m
Site C	Tx7-Rx3=4m;Tx8-Rx3=7m
Site D	Tx9-Rx4 =4m;Tx10-Rx4 =7m;Tx11-Rx4 =14m
Site E	Tx12-Rx5 =4m;Tx13-Rx5 =7m
Site F	Tx14-Rx6 =4m Tx15-Rx6 =7m;Tx16-Rx6 =14m

Chapter 4

Number of Array Element, Array Spacing, Multi-polarization, Bandwidth and Propagation on UWB-MIMO Channel Capacity

In this chapter, the effects of number of array element, array spacing, propagation, array multi-polarization, and bandwidth on UWB-MIMO channel capacity are explored by indoor measurements.

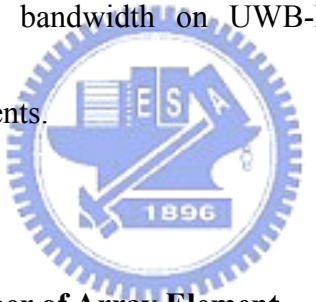

4.1 Array Spacing and Number of Array Element

Figs. 4-1 (a), (b) and (c) show mxn MIMO channel capacity versus array spacing with no.6 PA at Site A (LOS) and m or n =1-4 when d = 4m, 7m, and 14m, respectively. It seems that the capacity increases as the elements spacing increases in the LOS situation, which is due to the increase of de-correlation effect as the spacing increases. This incremental is also increases with the propagation distance or number of array element, which is also due to the increase of de-correlation effect. It is noted that this incremental saturates asymptotically when the array spacing is larger than 0.7 λ or 0.8

λ (It is named as the saturation length). It is found that the array spacing has not much effect on the capacity in LOS situation especially when the number of array element is small such as m or n = 1 or 2. However, when the number of array element is large and the total array length is also large, the overall de-correlation effect due to array spacing is increased and the MIMO capacity is increased. Figs. 4-2 (a), (b) and (c) show mxn MIMO channel capacity versus array spacing with no.6 PA at Site B (NLOS) and m or n =1-4 when d = 4m, 7m, and 14m, respectively. All the phenomena shown in last figure are also found here and become more obvious, which is due to the richness of multipath components in NLOS situations.

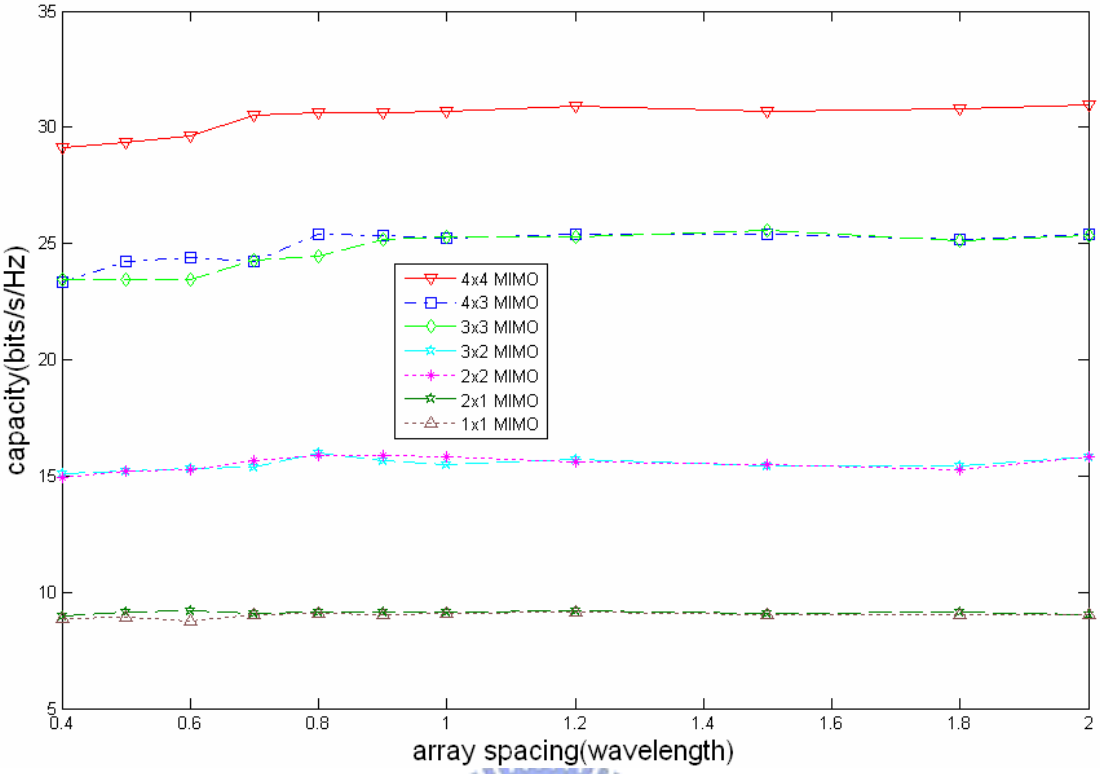

Fig. 4-1 (a) MIMO channel capacity versus array spacing at Site A with PA no.6 for SISO and mxn MIMO cases, where d=4m.

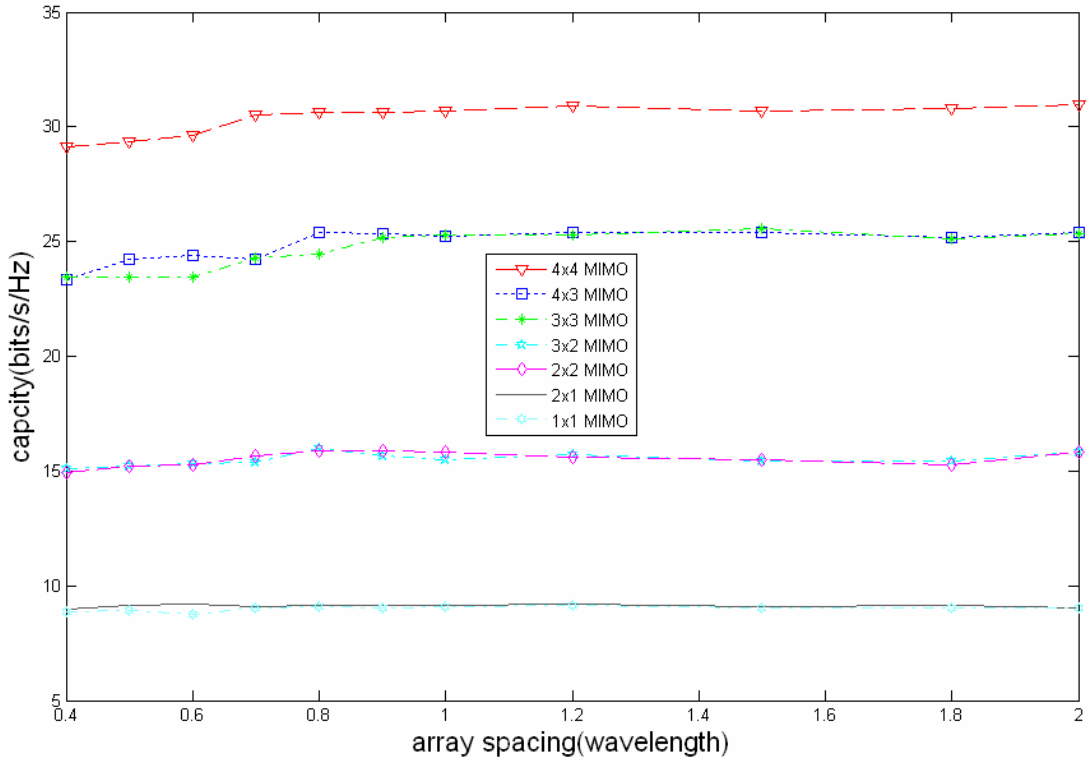

Fig. 4-1 (b) MIMO channel capacity versus array spacing at Site A with PA no.6 for SISO and mxn MIMO cases, where d=7m.

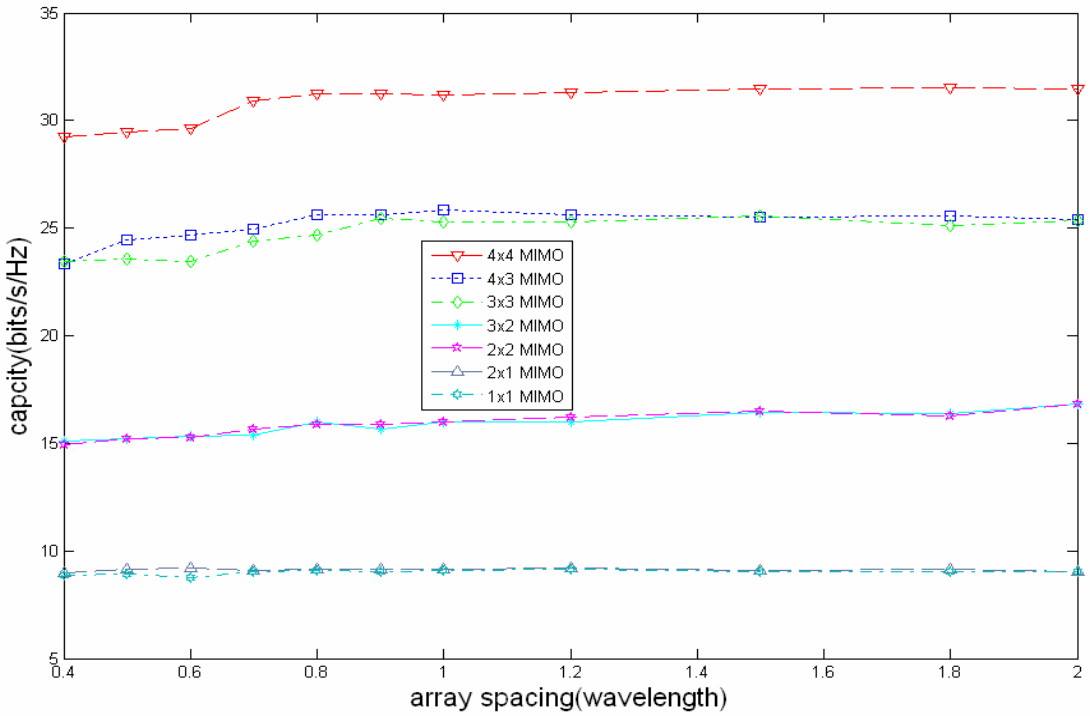

Fig. 4-1(c) MIMO channel capacity versus array spacing at Site A with PA no.6 for SISO and mxn MIMO cases, where d=14m.

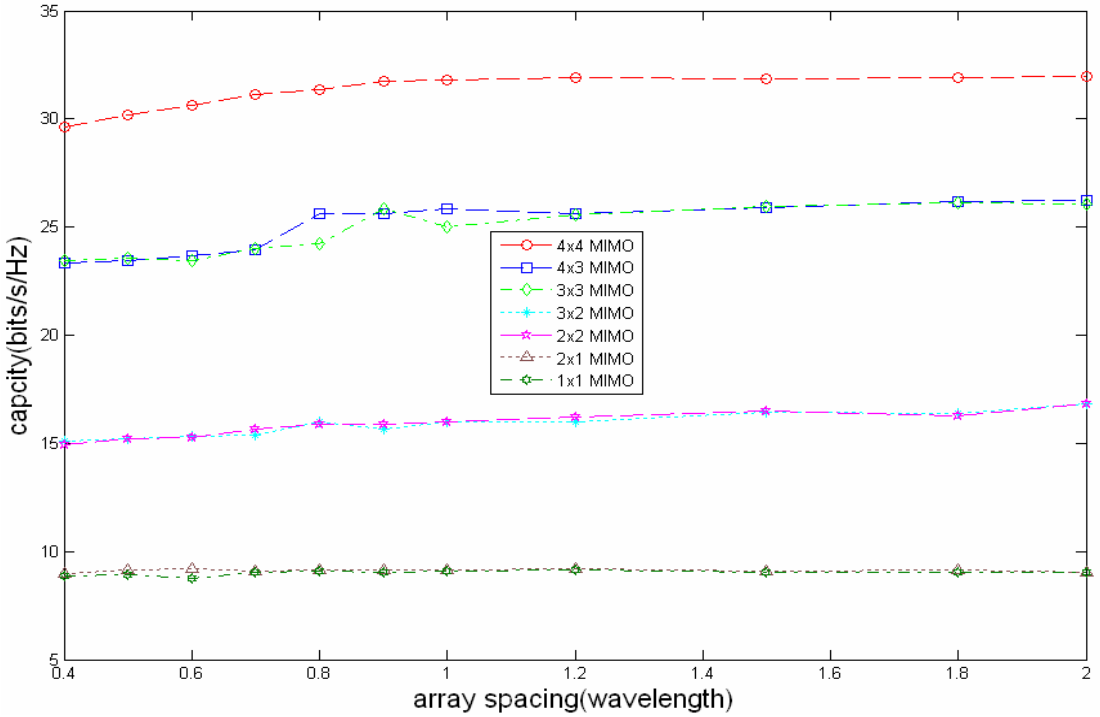

Fig. 4-2 (a) MIMO channel capacity versus array spacing at Site B (NLOS) with PA no.6 for SISO and mxn MIMO cases, where d=4m.

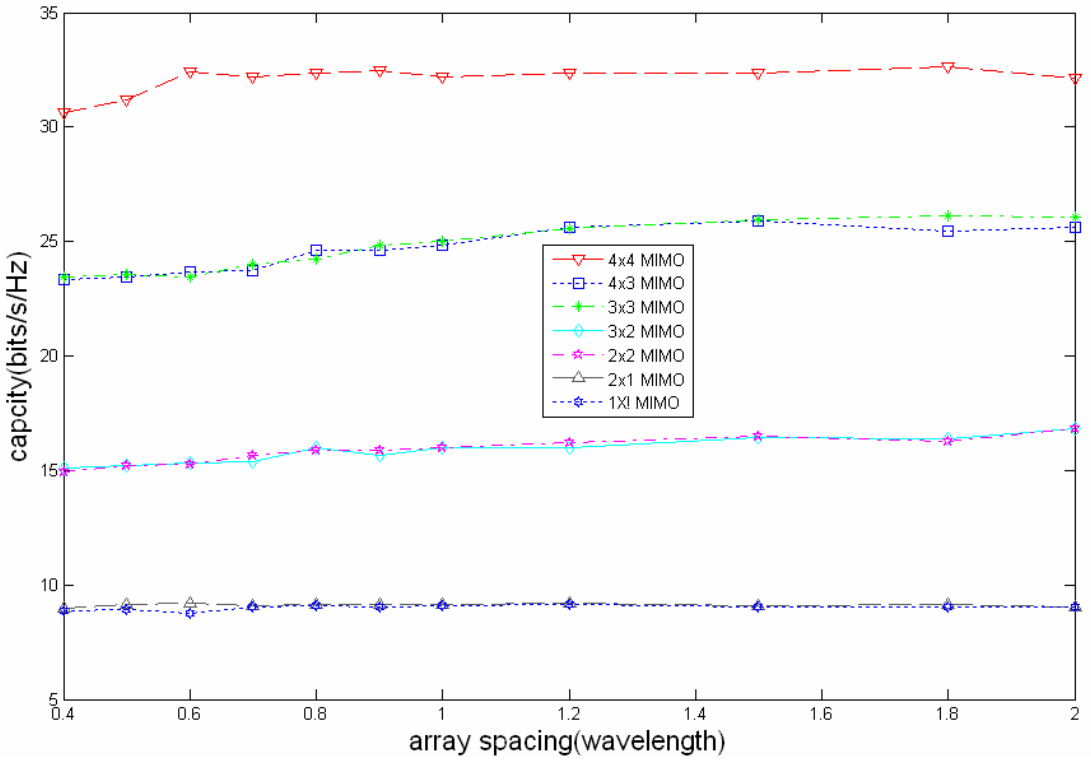

Fig 4-2 (b) MIMO channel capacity versus array spacing at Site B with PA no.6 for SISO and mxn MIMO cases, where d=7m.

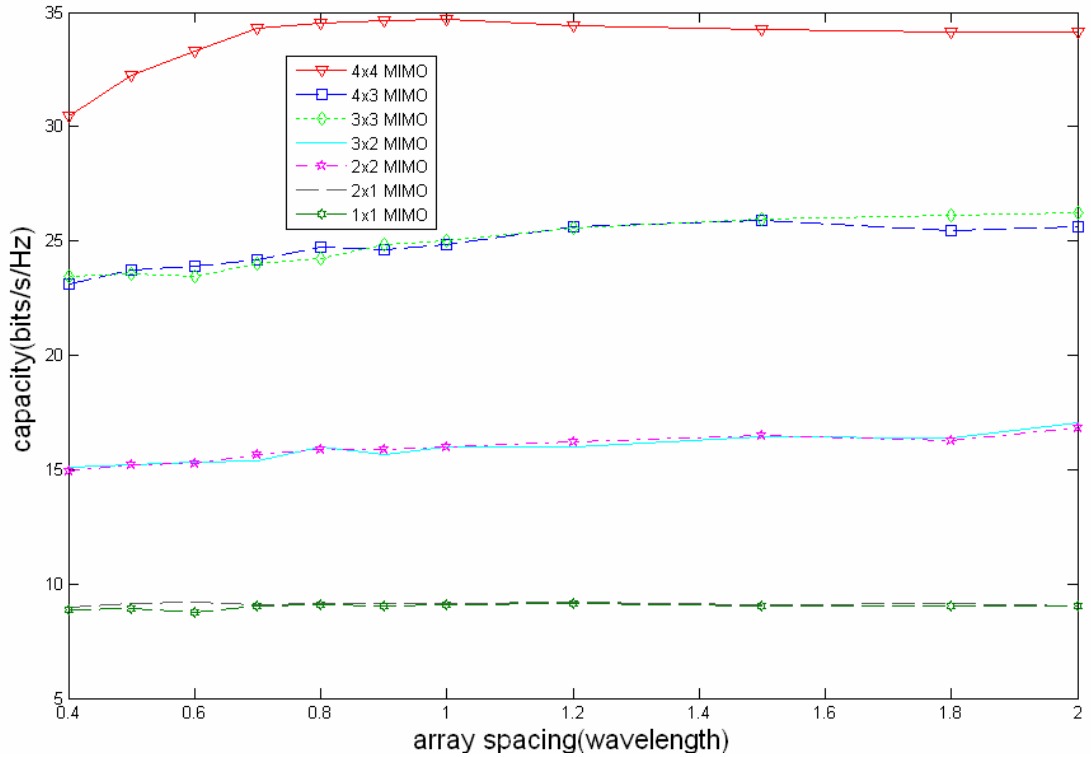

Fig 4-2 (c) MIMO channel capacity versus array spacing at Site B (NLOS) with PA no.6 for SISO and mxn MIMO cases, where d = 14m.

4.2 Multi-polarization effect

Figs. 4-3 and 4-4 illustrate MIMO capacity versus mxn array number for different polarization arrangements at Site A (LOS) and Site B, respectively. with array spacing = 0.8 wavelengths. From the figures, a well-known phenomenon is observed that the MIMO capacity is increased with m or n. It is noted that polarization mismatch can increase the capacity, which is validated by comparing the case of PA no.1 or PA no.2 (polarization mismatch) with PA no.6. It is noted this effect may be enhanced by increasing the propagation distances, which is revealed by comparing Fig. 4.3 (a) with Fig. 4.3 (b) or comparing Fig. 4.4 (a) with Fig. 4.4 (b).

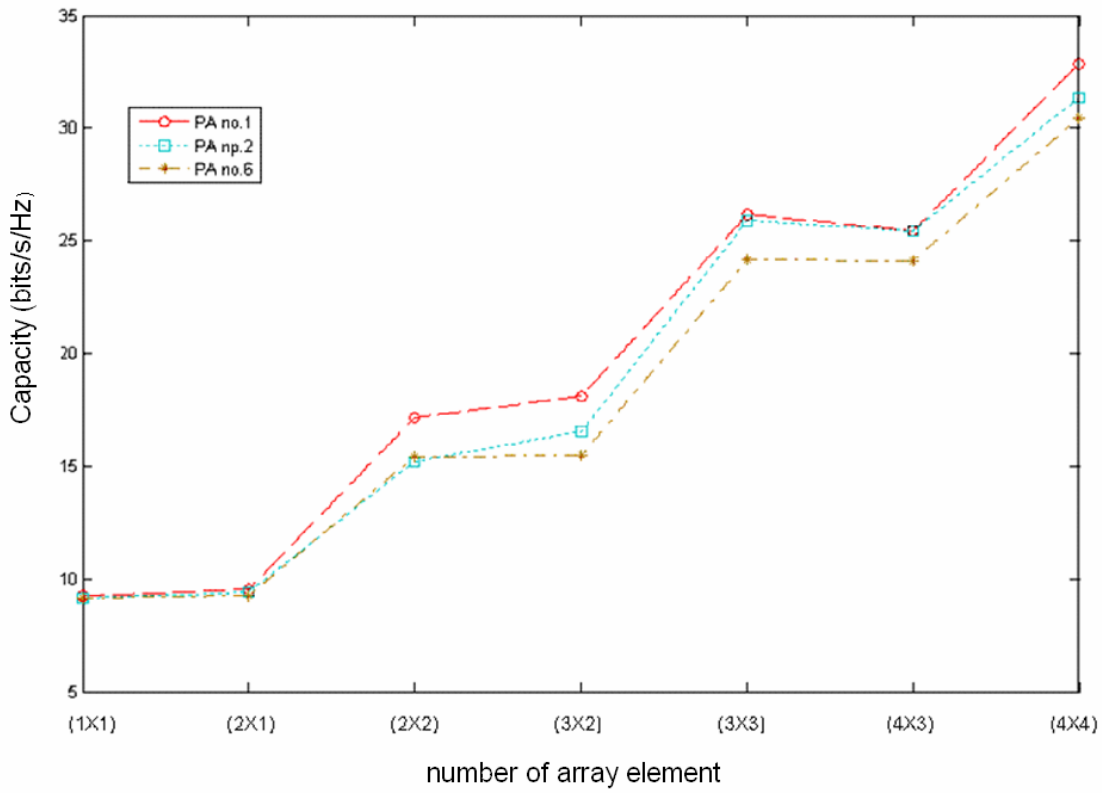

Fig. 4-3 (a) Capacity versus mxn array number for different polarization arrangements at Site A (LOS) with array spacing = 0.8 wavelengths and d=4m.

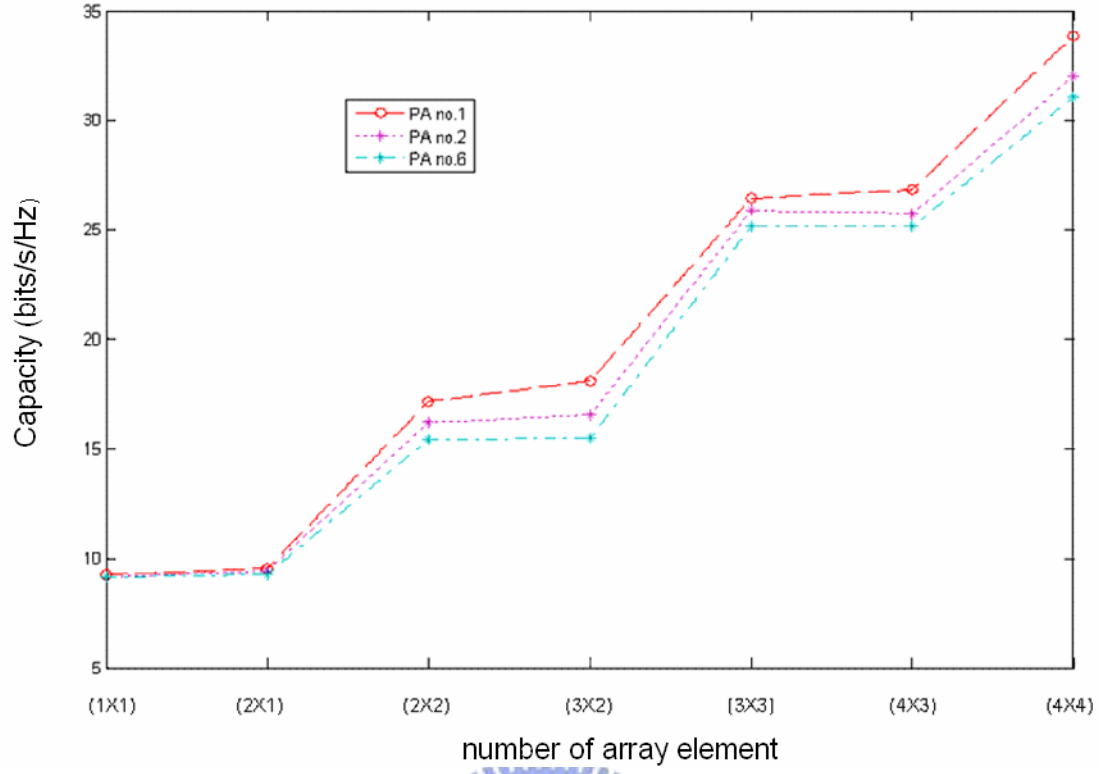

Fig.4-3 (b) Capacity versus mxn array number for different polarization arrangements at Site A (LOS) with array spacing = 0.8 wavelengths and d=14m.

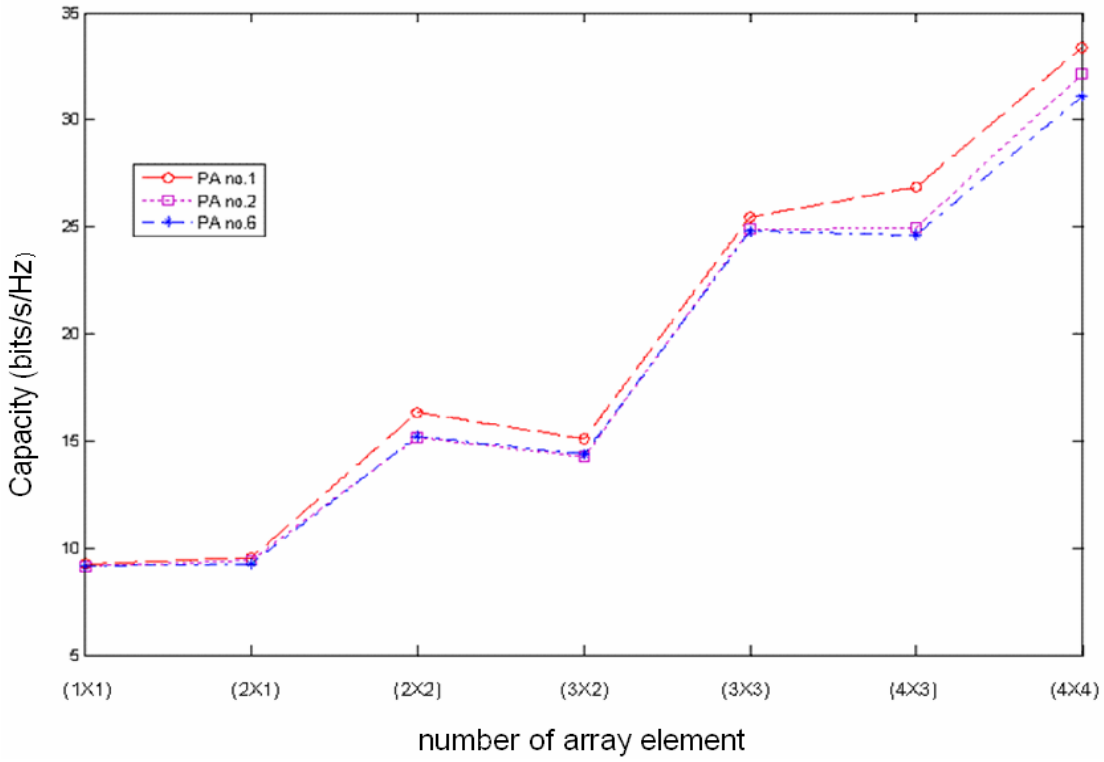

Fig.4-4 (a) Capacity versus mxn array number for different polarization arrangements at Site B (NLOS) with array spacing = 0.8 wavelengths and d = 4m.

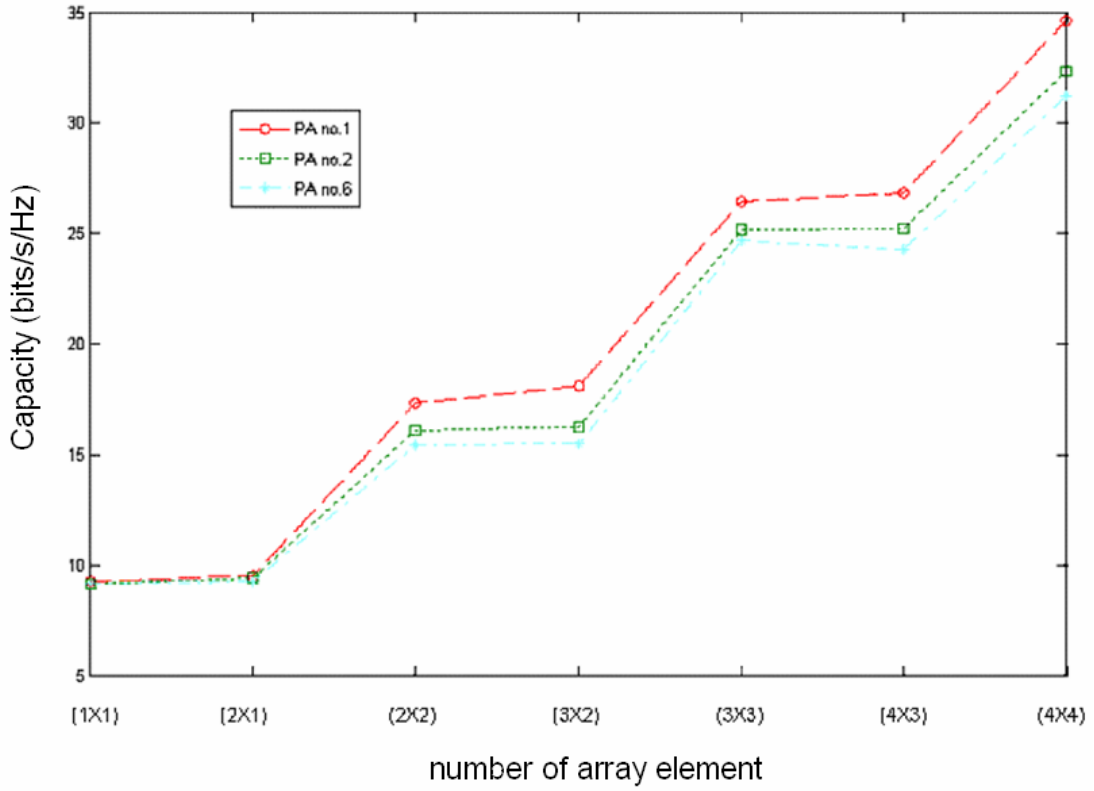

Fig.4-4 (b) Capacity versus mxn array number for different polarization arrangements at Site B (NLOS) with array spacing = 0.8 wavelengths and d=14m.

4.3 Multi-polarization and Antenna Spacing Coupling Effects

In previous sections, we have demonstrated that the multi-polarization and increasing of array spacing can both improve MIMO channel capacity. In this section, coupling effects of multi-polarization and array spacing are explored. Fig. 4-5 and Fig. 4-6 show 4x4 MIMO capacity versus arrays spacing at Sites A (LOS) and B (NLOS), respectively. Here, polarization arrangements no.1-no.7 are considered. It is found that mismatch polarization can decrease the saturation length to 0.7 or 0.8 wavelengths.

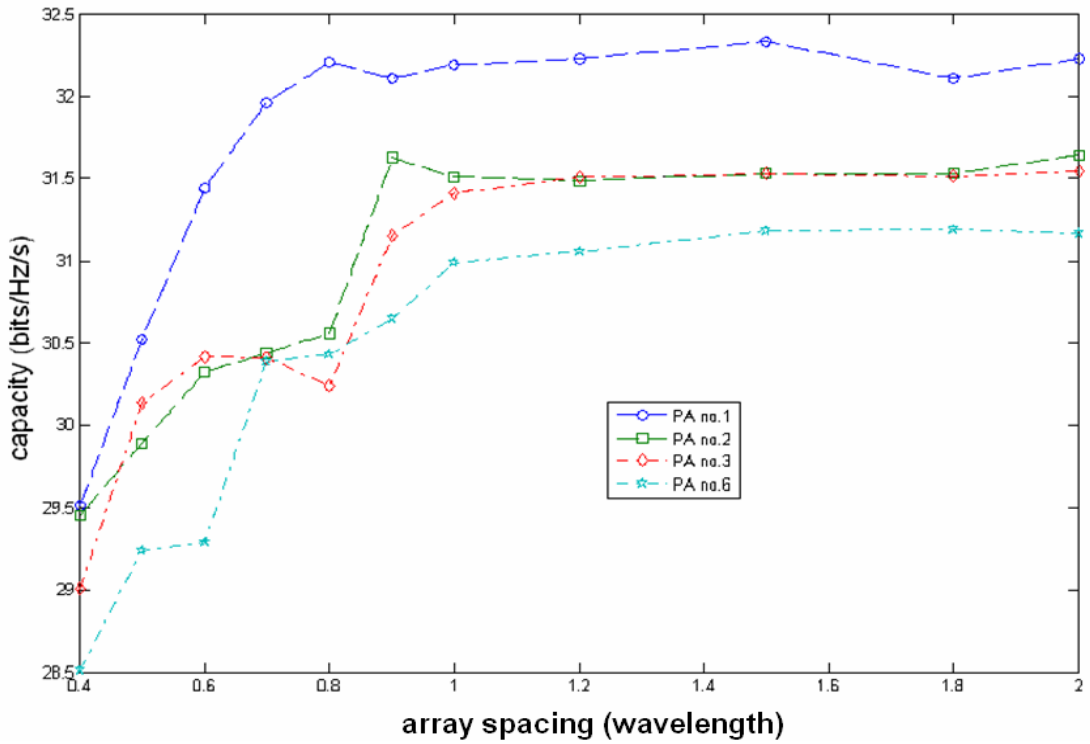

Fig. 4-5 4x4 MIMO capacity versus arrays spacing at site A (LOS) with d=14m. Here, polarization arrangements no.1-no.3 and no.6 are considered.

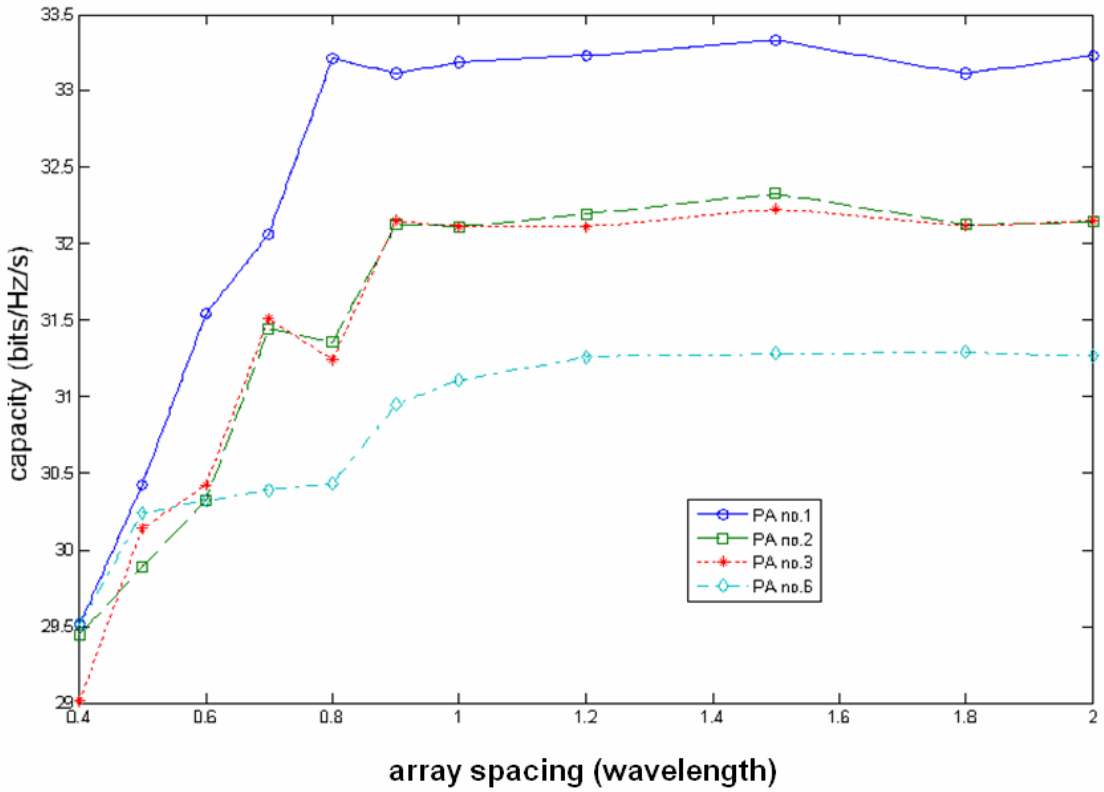

Fig.4-6 4x4 MIMO capacity versus arrays spacing at Site B (NLOS) with d=14m. Here, polarization arrangements no.1-no.3 and no.6 are considered.

4.4 Capacity v.s. Frequency

In this section we analyze how the operating frequency affects the 4X4UWB-MIMO capacity. We carry out the measurement in NOLS and LOS situations (scenarios I/II/III/IV) with PA no. 6. The antenna spacing is 0.5 wavelength. Frequency is swept from 3 GHz to 5 GHz (central frequency is 4 GHz) during the measurement. Figs. 4-7 (a)-(d) show the measured frequency responses of 4x4 MIMO capacity at Sites C - F. It seems that the measured frequency responses of 4x4 MIMO capacities at LOS situations have a similar distribution, which is different from that in NLOS situations. Fig.4.8 also demonstrates similar phenomena.

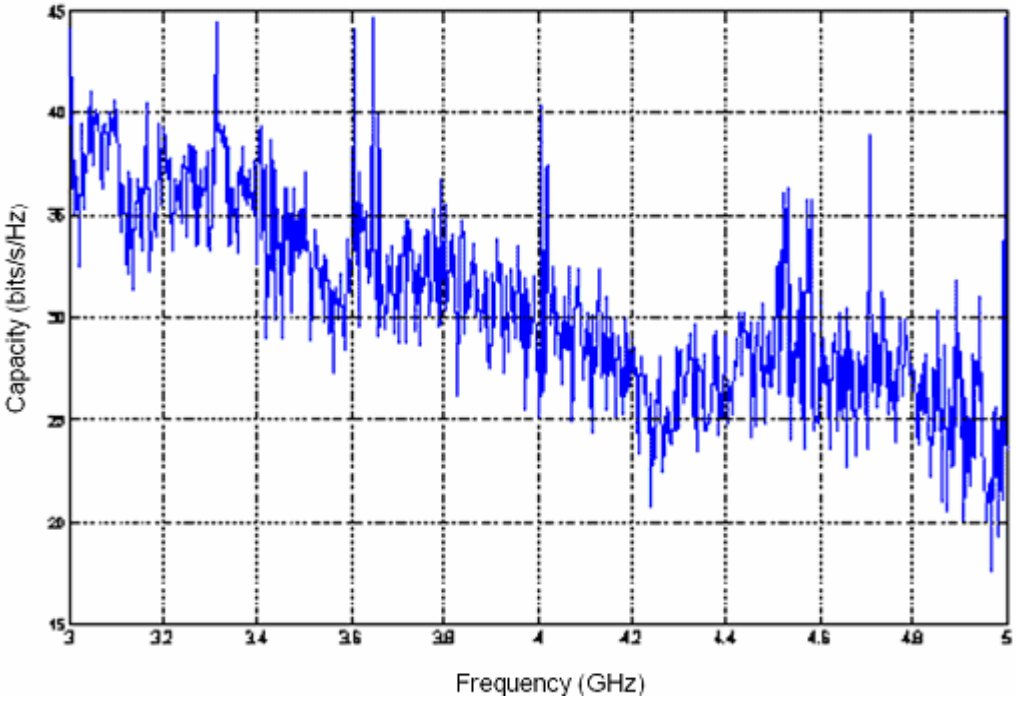

Fig 4-7 (a) 4x4 MIMO channel capacity versus operating frequency Tx-Rx (d = 4m, Site C, NLOS)

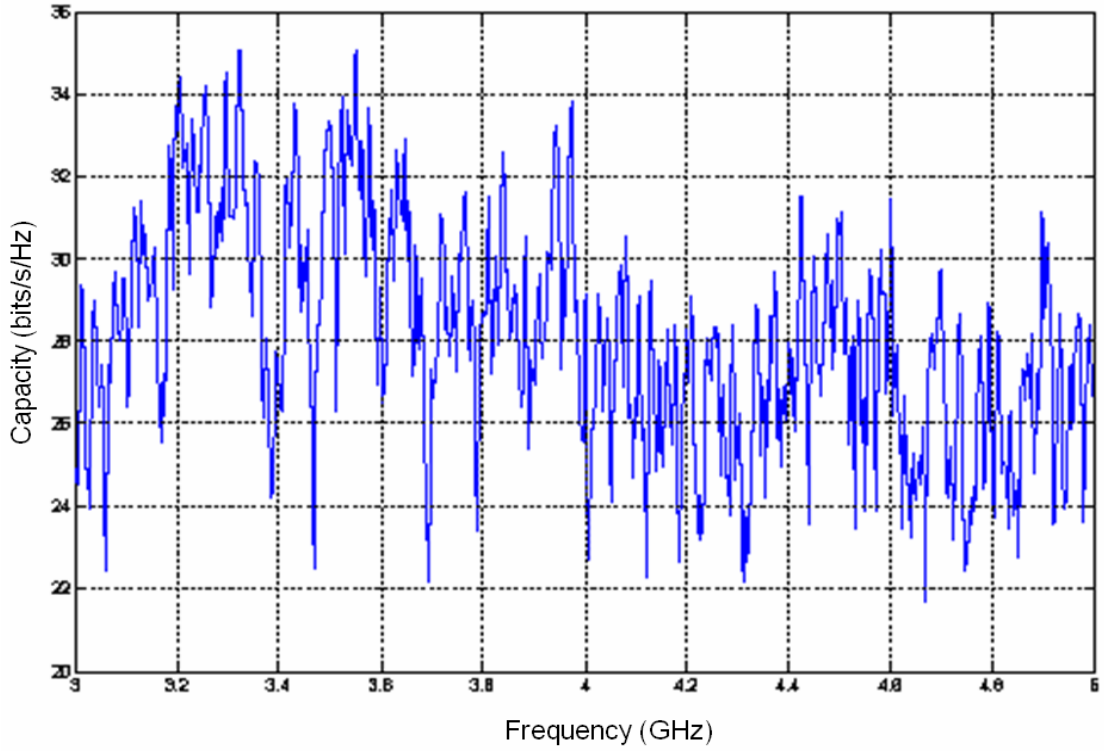

Fig 4-7 (b) 4x4 MIMO channel capacity versus operating frequency Tx-Rx (d=4m, site D, LOS)

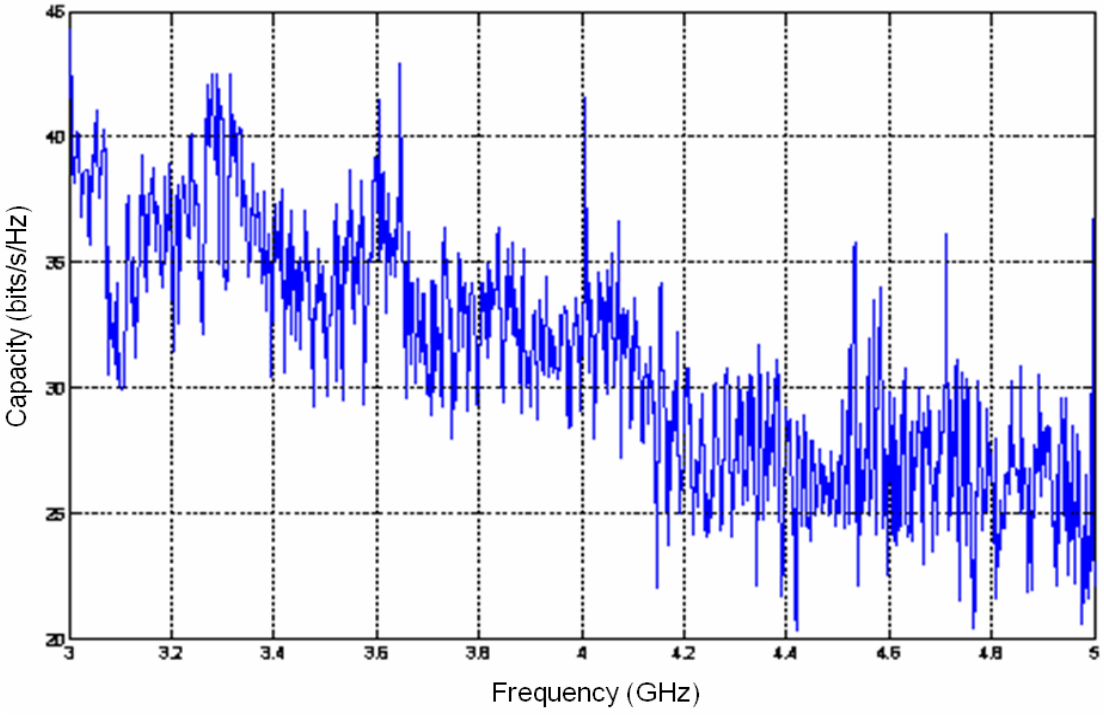

Fig 4-7 (c) 4x4 MIMO channel capacity versus operating frequency Tx-Rx (d = 4m, site E, NLOS)

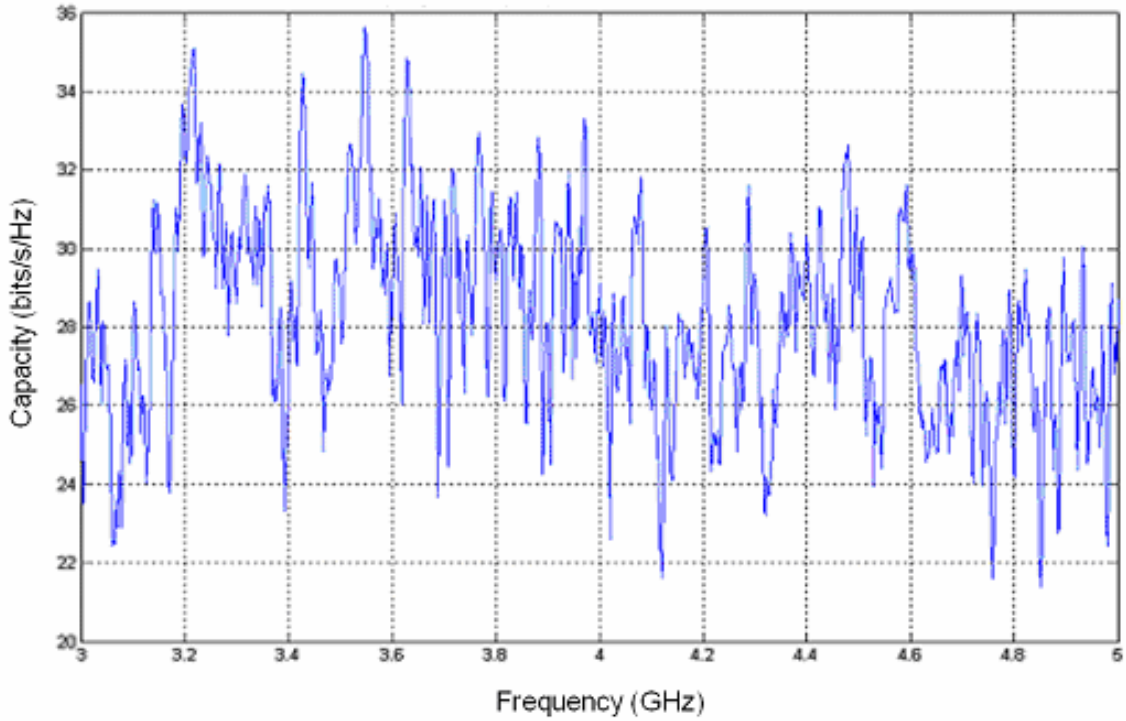

Fig 4-7 (d) 4x4 MIMO channel capacity versus operating frequency Tx-Rx (d = 4m, site F, LOS)

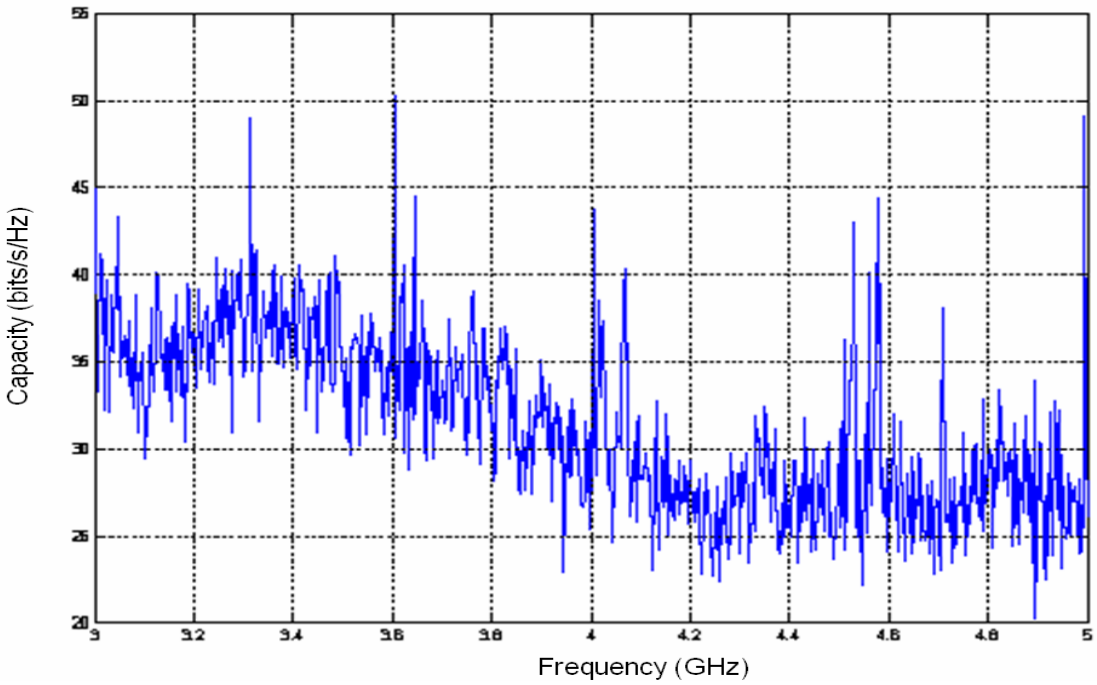

Fig. 4-8 (a) 4x4 MIMO channel capacity versus operating frequency Tx-Rx (d = 7m, site C, NLOS)

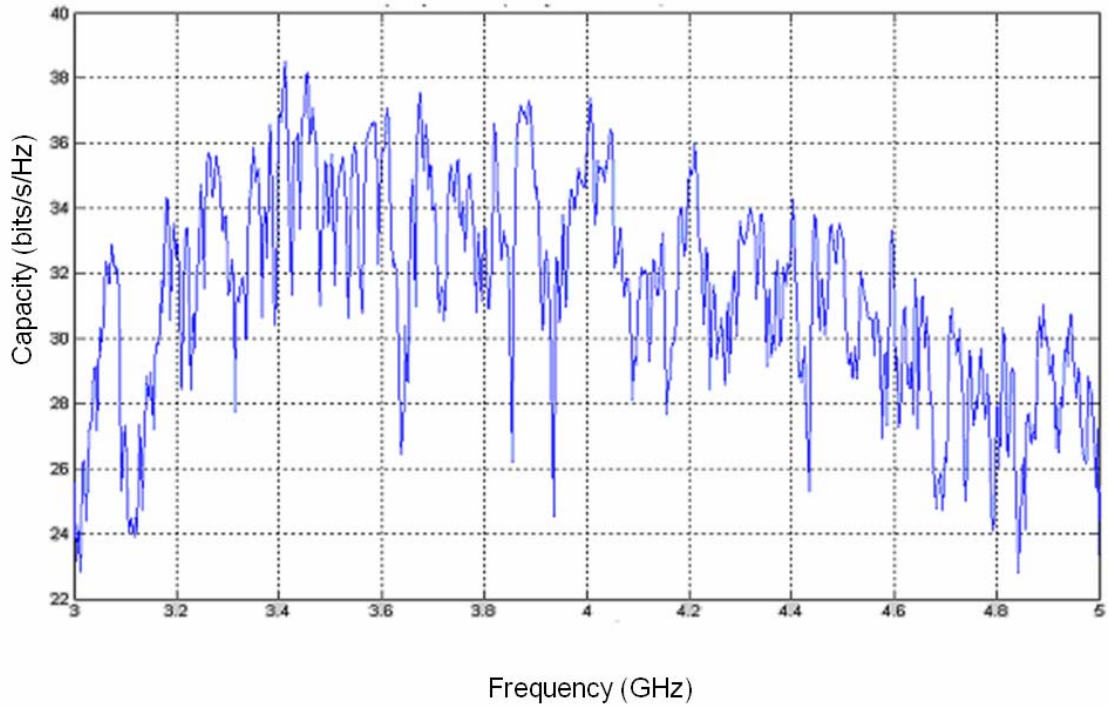

Fig. 4-8 (b) 4x4 MIMO channel capacity versus operating frequency Tx-Rx (d=7m, site D, LOS)

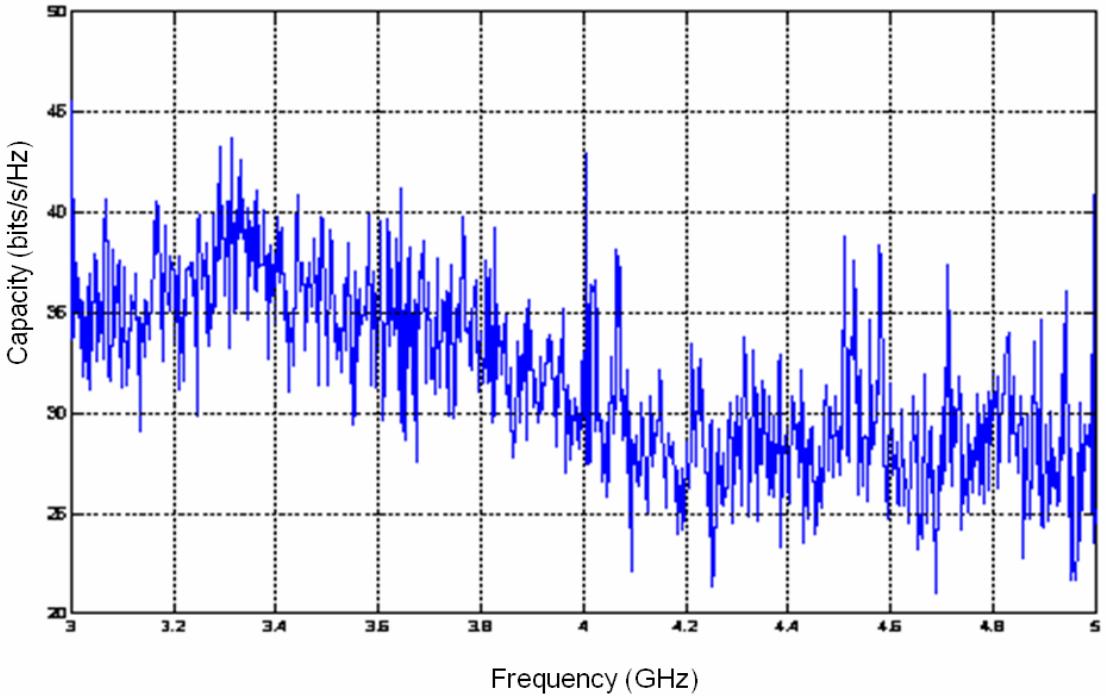

Fig. 4-8 (c) 4x4 MIMO channel capacity versus operating frequency Tx-Rx (d=7m, site E)

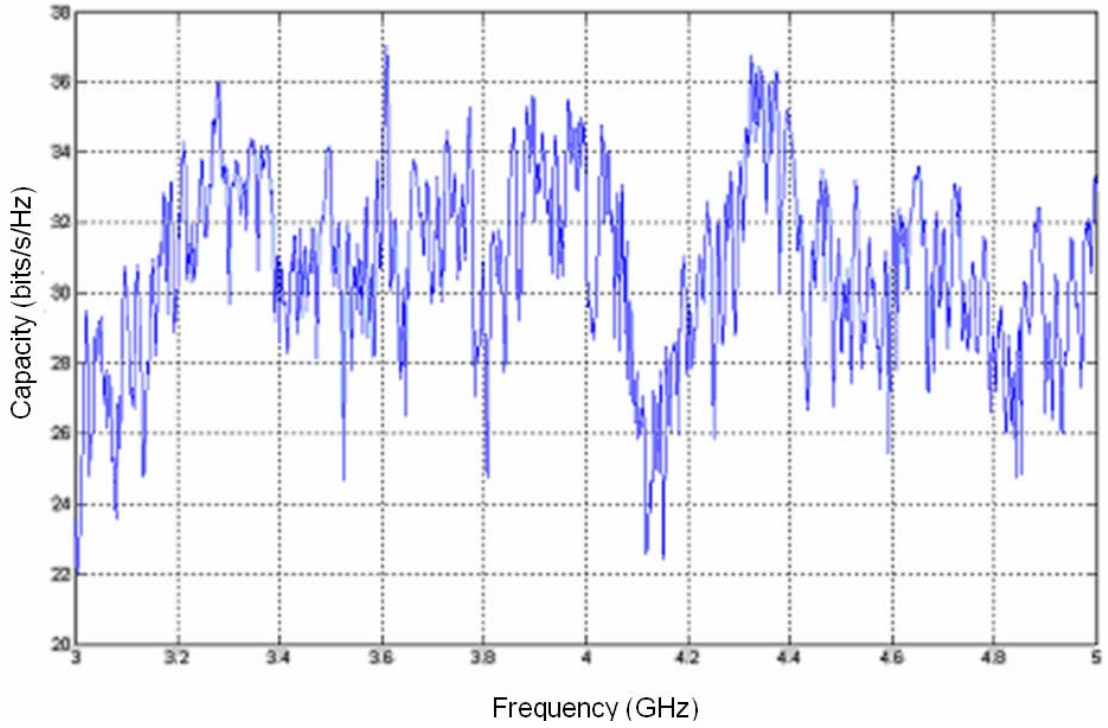

Fig. 4-8 (d) 4x4 MIMO channel capacity versus operating frequency Tx-Rx (d=7m, site F)

4.5 Bandwidth Effect

Here, 50 MHz, 100 MHz, 200 MHz, 500 MHz, 1GHz, and 2 GHz signal bandwidths are considered for measurements (carrier frequency is 4 GHz). Fig. 4-9 shows that a little difference when the signal bandwidth is changed. However, NLOS cases have larger capacity than LOS cases.

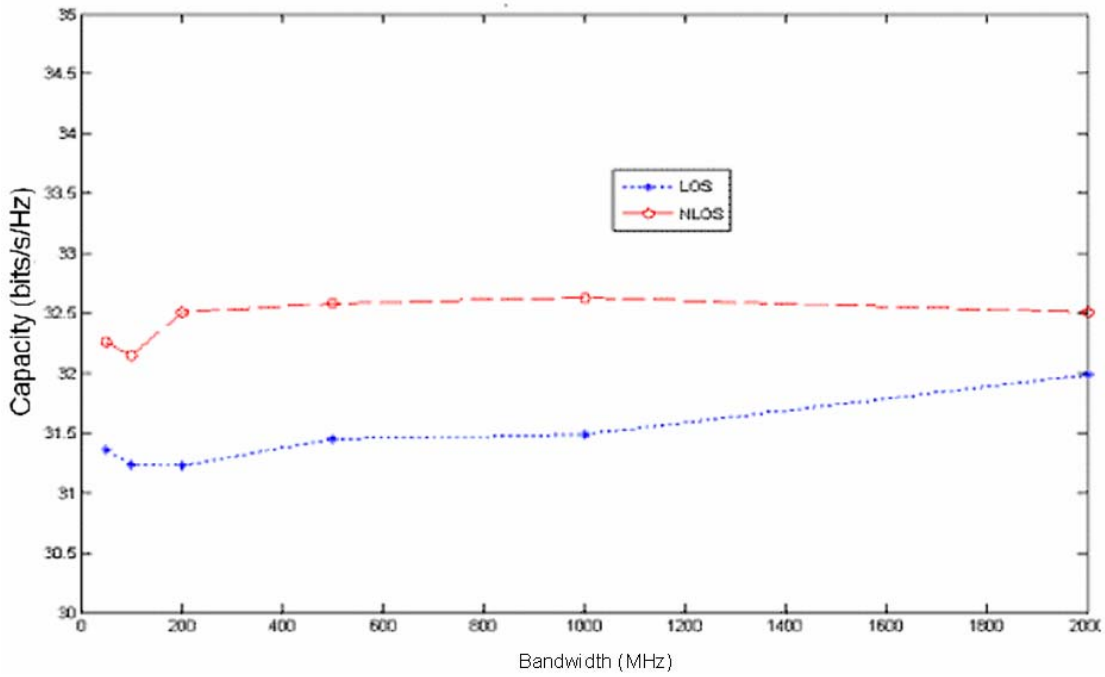

Fig. 4-9 4x4 MIMO capacity versus bandwidth for NLOS and LOS situations at Sites C-F.

4.6 Propagation Effect

Fig. 4-10 illustrates 4x4 MIMO capacity versus Tx-Rx distance at Sites A-F. It is noted that Sites A, D and F are LOS situations and Sites B, C and E are NLOS situations. The MIMO capacity is increased with the propagation distance and it seems to be saturated when the distance is large.

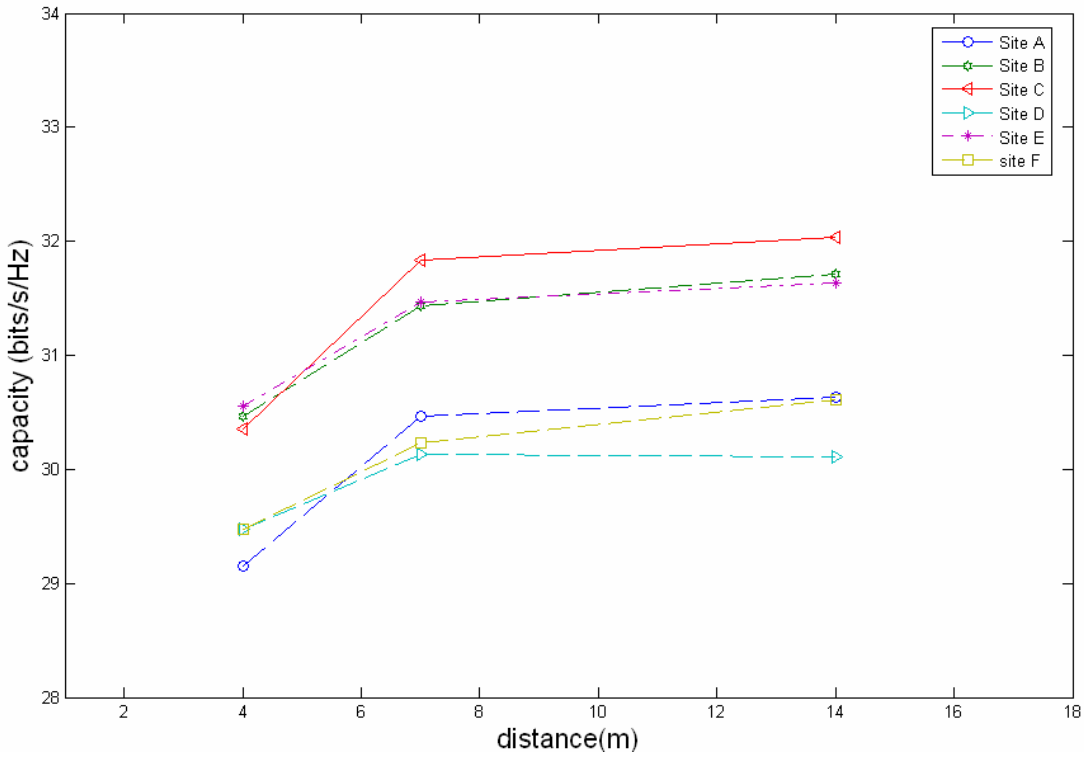

Fig.4-10 Capacity versus propagation range effect with PA no.1 in NLOS and LOS situations, where d = 4m ,7m ,and 14m.

Chapter 5

Spatio-Temporal Elliptical Propagation Modeling For Multi-Polarized MIMO Fixed Wireless Channels

This chapter addresses the extension of a stochastic geometry-based scattering model to analysis and design of multielement antenna systems in mobile fading channels including characteristics of (MIMO) multipolarized transmission.

5.1 Modeling of Multi-polarized MIMO Channels

The MIMO channel is completely described by a two-dimensional (2-D) ellipse spatial distribution of scatterers and the antenna configurations at both transmitter and receiver sides. Scatterers are specified by their locations and scattering properties. Antennas are defined by the array configuration (i.e., the relative location and polarization of each individual antenna). The multi-element antenna system is shown in Fig. 5-1 with m and n multi-polarized antenna elements.

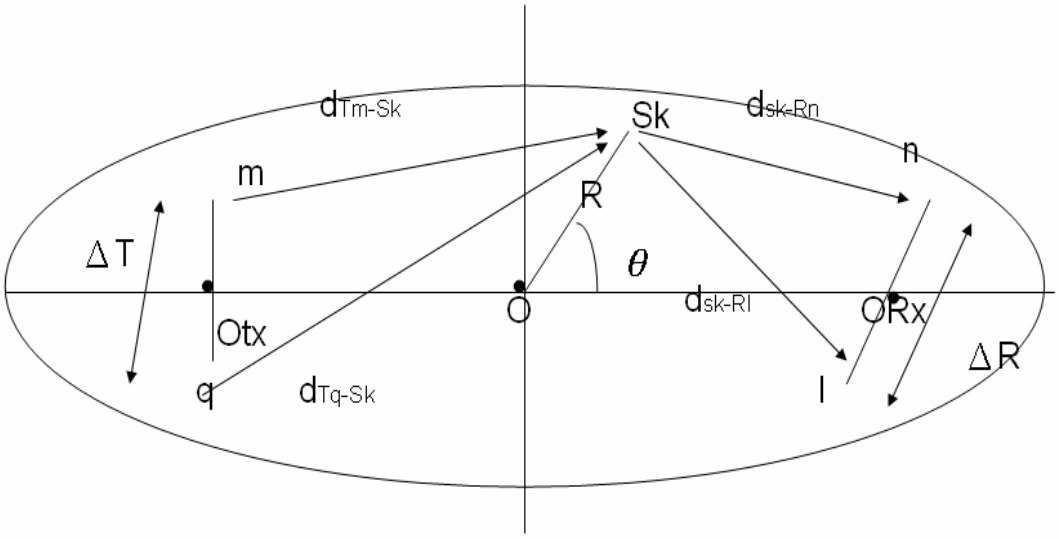

Fig.5-1 Geometrical configuration of a mxn channel with local scatterers around the Tx and Rx arrays

Based on Fig 5.1, the channel gain $h_{lp}(t)$ can be represented by $h_{lp}(t) = h_{lp}^{NLOS}(t) + h_{lp}^{LOS}(t)$. The Plane waves emitted from the array element m of Tx travel over paths with different lengths and after being scattered by local scatterers , impinge the array element Rx from different directions. Mathematical representation of this propagation mechanism results in the following expressions for the diffuse and the LOS components, identified by the superscripts NLOS and LOS, respectively. The scattering component of a transmission from Tx antenna m to Rx antenna n can be expressed as

$H_{mn}^{NLOS}(t)$

$$= \sum_{i=1}^{s} G(k)_{Tx,m} \cdot \frac{\exp[\frac{-j2\pi(d_{Tm} - S_k)}{\lambda}]}{(d_{Txm} - S_k)^{\gamma/2}} \cdot \frac{\exp[\frac{-j2\pi(dS_k - R_n)}{\lambda}]}{(d_{Sk} - R_n)^{\gamma/2}} \cdot \mathbf{\Omega}(k)_{mn}\, G(k)_{Rx,n} \qquad (5\text{-}1)$$

where

- λ is the wavelength;
- $G(k)_{Tx,m}$ is the amplitude gain of mth (Tx) antenna in the direction of the *k*th scatterer;
- $d_{Tml} - S_k$ is the distance from the mth Tx to the *k*th scatterer;
- $d_{sk} - R_n$ is the distance from the *k*th scatterer to the *n*th receive antenna;
- γ (= 2 in this paper) is the power–law attenuation coefficient applicable to each individual effective path;
- $G(k)_{Rx,n}$ is the amplitude gain of the *n*th (Rx) antenna in the amplitude of the *k*th scatterer;
- $\mathbf{\Omega}(k)_{mn}$ is the (m, n) element of the global scattering matrix due to *k*th scatterer, which includes all polarization effects(scattering and antenna **XPD**). Here, **Ω** will be defined later.

With Eq. (5-1), the LOS component is given by (5-2)

$$H_{mn}^{LOS}(t) = \sum_{i=1}^{s} G(0)_{Tx,m} \cdot \frac{\exp[\frac{-j2\pi(d_{Txm} - R_n)}{\lambda}]}{(d_{Txm} - R_n)^{\gamma/2}} \cdot \cdot \mathbf{\Omega}(k)_{mn} G(0)_{Rx,n} \qquad (5\text{-}2)$$

For including the multi-polarized effect, a 2X2 multi-polarized MIMO system is explored first, then extending to any m x n system. The MIMO system is indicated in

Fig. 5-2, and the array spacings at the transmitting and receiving sides are denoted as Δt and Δr, respectively. It is important to note that both lth (l = 1, 2) antennas have the same polarization while, at each side, antennas 1 and 2 are given orthogonal polarizations. The channel cross-polarization discriminations (XPDs) for receiving antennas 1 and 2 are defied as (with Eq. (5-3))

$$\mathbf{XPD}_1 = |H_{11}|^2/|H_{21}|^2 \text{ and } \mathbf{XPD}_2 = |H_{22}|^2/|H_{12}|^2 \qquad (5\text{-}3)$$

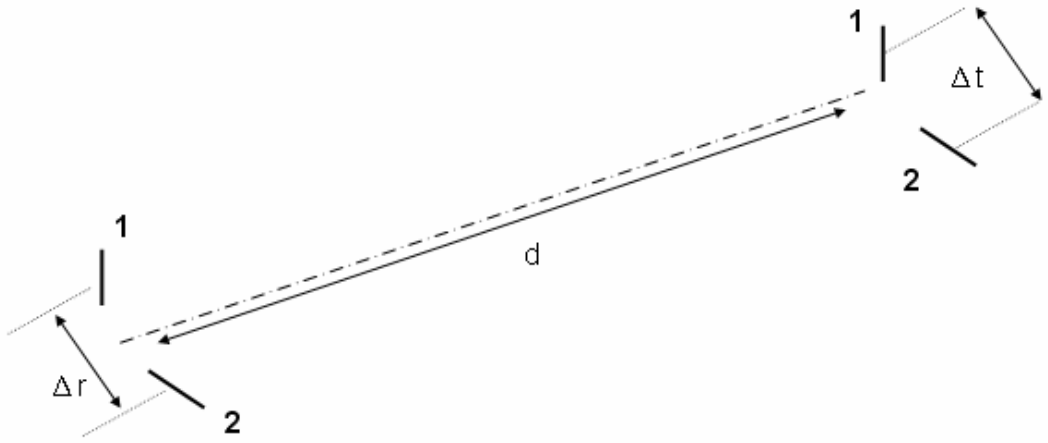

Fig.5-2 The geometry of a 2x2 multi-polarized MIMO antennas. Antennas 1 and 2 at the transmitting site or receiving site are orthogonal polarizations.

The model of the scatter component relies on the description of the matrix effective reflection coefficient $\mathbf{\Omega}$ associated to each scatter .The latter can be expressed as a product of the antenna polarization matrix **C** and the scattering matrix $\mathbf{\Gamma}$

$$\mathbf{\Omega} = \mathbf{C} \cdot \mathbf{\Gamma} \qquad (5\text{-}4)$$

where **C** is the antenna-polarization matrix (with diagonal elements being normalized to unity)

$$\mathbf{C} = \begin{bmatrix} 1 & \dfrac{1}{x_{a,1}\exp(j\Phi a,1)} \\ \dfrac{1}{x_{a,2}\exp(j\Phi a,2)} & 1 \end{bmatrix} . \qquad (5\text{-}5)$$

where, $X_{a,n}\ \exp(j\Phi a,n)$ (n = 1,2) is the *n*th receive antenna **XPD**. It is a complex value, With Xa,n ≥ 1 depending on the antenna design and Φa,n being an arbitrary phase shift assumed to be uniformly distributed .If both antennas have similar **XPD**s, then $Xa,_1 = Xa,_2 = Xa$.

Note that for unipolarized transmission, (5-4) is still valid, $\mathbf{\Omega}(k) = \mathbf{\Omega_{11}(k)}$ or $\mathbf{\Omega}(k) = \mathbf{\Omega_{22}}(k)$, depending on the antenna polarization.

In order to obtain a model of **Γ** for any polarization scheme, we will derive the statistical properties of the scattering matrix $\mathbf{\Gamma_0}$ for the particular case of a $0^\circ/90^\circ$ Scheme:

$$\mathbf{\Gamma_0} = \begin{bmatrix} \Gamma_{vv} & \Gamma_{vh} \\ \Gamma_{hv} & \Gamma_{hh} \end{bmatrix} \qquad (5\text{-}6)$$

where subscripts *v* and *h* refer, respectively, to vertical and horizontal polarizations. From the scattering matrix $\mathbf{\Gamma_0}$, it is straight forward to obtain the scattering matrix **Γ** corresponding to any orthogonal scheme, as shown in

$$\mathbf{\Gamma} = \begin{bmatrix} \Gamma_{vv}\cos^2\Psi + \Gamma_{hh}\sin^2\Psi + (\Gamma_{vh}+\Gamma_{hv})\cos\Psi\sin\Psi & (\Gamma_{vv}-\Gamma_{hh})\cos\Psi\sin\Psi + \Gamma_{vh}\cos^2\Psi - \Gamma_{hv}\sin^2\Psi \\ (\Gamma_{vv}-\Gamma_{hh})\cos\Psi\sin\Psi + \Gamma_{vh}\cos^2\Psi - \Gamma_{hv}\sin^2\Psi & \Gamma_{vv}\sin^2\Psi + \Gamma_{hh}\cos^2\Psi_R + (\Gamma_{vh}+\Gamma_{hv})\cos\Psi\sin\Psi \end{bmatrix} \quad (5\text{-}7)$$

where ψ is one of the polarization angles of the scheme relative to the vertical direction.

The only remaining unknown is the matrix $\mathbf{\Gamma_0}$**.** The latter can be statistically described with the help of electromagnetic theory and ray-tracing simulation scenarios described in [30]. We have calculated, using the electromagnetic model of [30] and a typical built-up area, the complex scattering coefficient on each individual single-scattered multipath for a large number of transmit and receive locations and for each of the two polarizations(horizontal and vertical) at a frequency of 5.5 GHz. In such scenarios, single-scattering coefficients $\mathbf{\Gamma_{vv}}$ **,** $\mathbf{\Gamma_{hh}}$ **,** $\mathbf{\Gamma_{hv}}$ **,** $\mathbf{\Gamma_{vh}}$ can be calculated using the Fresnel theory and the uniform theory of diffraction (UTO), as detailed in the Appendix. A statistical analysis of these four coefficients yields the following results.

1) $|\Gamma_{vv}|^2$ is logonormally distributed, with the additional condition that $0 \leq |\Gamma_{vv}| \leq 1$.

2) Argument of Γ_{vv} is uniformkly distributed over $[0,2\pi]$.

3) Γ_{vv} can be expressed as a hpase shifted and attenuated version of Γ_{vv}

$$\Gamma_{\mathbf{hh}} = \Gamma_{\mathbf{vv}} \cdot \frac{\exp(-j\varepsilon)}{\beta} \quad (5\text{-}8)$$

where ε is a zero-mean Gaussian-distributed variable (with standard deviation of about 0.3, as found from the statistical analysis) and β is the gain imbalance between vertical and horizontal scattering amplitudes. The imbalance β results from the fact that the major propagation mechanisms, identified in [31] as street waveguiding (i.e., reflection by vertical walls) and rooftop diffraction by horizontal wedges, are polarization selective in favor of the vertical polarization. This effect has been highlighted by various measurement results [32], [33], [34] and by electromagnetic simulation results [30].

4) $|\Gamma_{hv}|$ and $|\Gamma_{vh}|$ are similarly proportional to $|\Gamma_{vv}|$ and $|\Gamma_{hh}|$; the proportionality factors are denoted as χ_{hv} and χ_{vh} as

$$\Gamma_{hv} = \Gamma_{vv} \cdot \frac{\exp(-j\Phi_{hv})}{\chi_{hv}} \qquad (5\text{-}9)$$

$$\Gamma_{vh} = \Gamma_{hh} \cdot \frac{\exp(-j\Phi_{vh})}{\chi_{vh}} \qquad (5\text{-}10)$$

with Φ_{hv} and Φ_{vh} independently uniformly uniformly distributed over $[0,2\pi]$.Conclusions 2)-4) are fairly intuitive and reflect three observed mechanisms i.e., the existence of a vertical-to- horizontal gain imbalance, a scattering **XPD**, and a random phase shift in the cross-polarization terms.

Since $|\Gamma_{vv}|^2$ is lognormally distributed, the distribution of $|\Gamma_{vv}|$ is given by

$$T_{|\Gamma_{vv}|}(|\Gamma_{vv}|) = \frac{1}{2\,|\,\Gamma_{vv}\,|^3\sqrt{2\pi\sigma^2}}\exp[-\frac{\log^2[\frac{|\,\Gamma_{vv}\,|^2}{\mu}]}{2\sigma^2}] \qquad (5\text{-}11)$$

Where logμ is the mean value of $\log|\Gamma_{vv}|^2$ and σ is the standard deviation of $\log[\,|\Gamma_{vv}|^2/\mu]$.Based on the ray-tracing simulation results, (μ,σ) are assigned the values . Furthermore, β^2 and χ^2 are alos found to be lognormally distributed.The parameters of these lognormal distributions have been inferred form physical simuations, yielding characteristic parameters equal ro (25,15) for the lognormal distribution of β^2 (yielding $E\{\beta^2\} = 8dB)^2$ and to (20, 0.5) for the lognormal distributions of χ_{vh}^2 and χ_{hv}^2 (yielding $E\{\chi_{vh}^2\} = E\{\chi_{vh}^2\} = 18.5dB$).

2) Dominant Component : The dominant component results from both an LOS component and various coherent (nonfading) scattered contributions. The dominantRicean component H_c of the channels is subsequently written as

$$H_c = H_{LOS} + H_{NLOS} \qquad (5\text{-}12)$$

The channel matrix corresponding to the dominant contribution is written as H_{LOS} is the LOS component.

Based on the 2 x 2 channel model, the modeling of any multipolarized MIMO channel

is straightforward. Consider, for example, the scatter component between two antennas, with respective polarizations relative to the vertical direction given by ψ_T and ψ_R. The channel between these antennas is calculated as in (5-4).The effective scattering coefficient is obtained by generalizing (5-5) and (5-8) as

$$\Omega\psi_T\psi_R = [1 \quad \frac{1}{\chi_a}\exp(j\Phi_a)] \cdot \begin{bmatrix} \cos\Psi_R & \sin\Psi_R \\ \sin\Psi_R & -\cos\Psi_R \end{bmatrix} \cdot \mathbf{\Gamma_0} \cdot \begin{bmatrix} \cos\Psi_T \\ \sin\Psi_T \end{bmatrix} \quad (5\text{-}13)$$

5.2 Validation of the proposed model

For analyzing multi-polarized M×N MIMO indoor radio channels, we propose a channel model to simulate its characteristic. The model is based on the Spatio-Temporal Elliptical Propagation model for presenting geometry scheme, Including propagation effect, antenna spacing effect and multipolarized antenna effect, etc, the default values of parameters for simulation are listed in Table 5-1.

Now, we demonstrated the simulation to compare measurement in NLOS and LOS with PA no.1-7 (Fig 5-3).

Table 5-1 Parameter set-up for simulation

Simulation parameter	Default value
Frequecny [GHz]	5.5
Array spacing (wavelengths)	0.4-2.0
Propagation range(m)	7
Local scatterers numbers	10
Antenna XPD Xa, [dB]	13
SNR [dB]	30

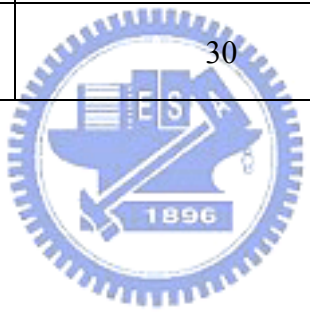

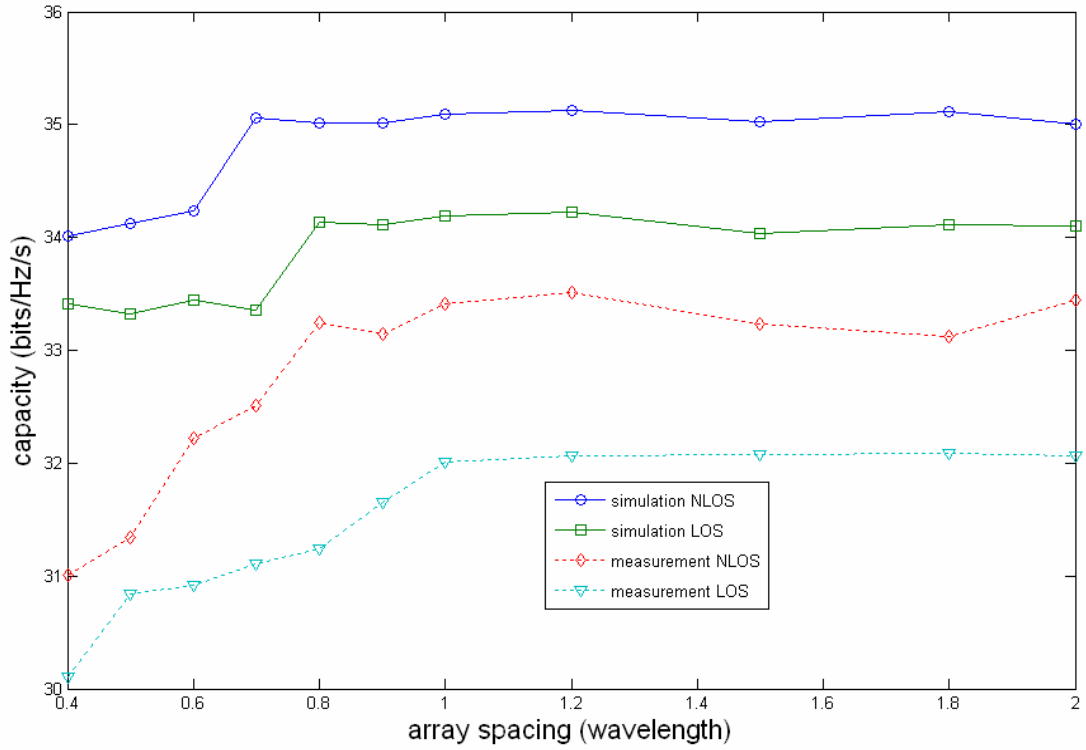

Fig. 5-3 (a) Capacity versus array spacing simulation and measurement (PA no. 1) d=7m (NLOS, LOS)

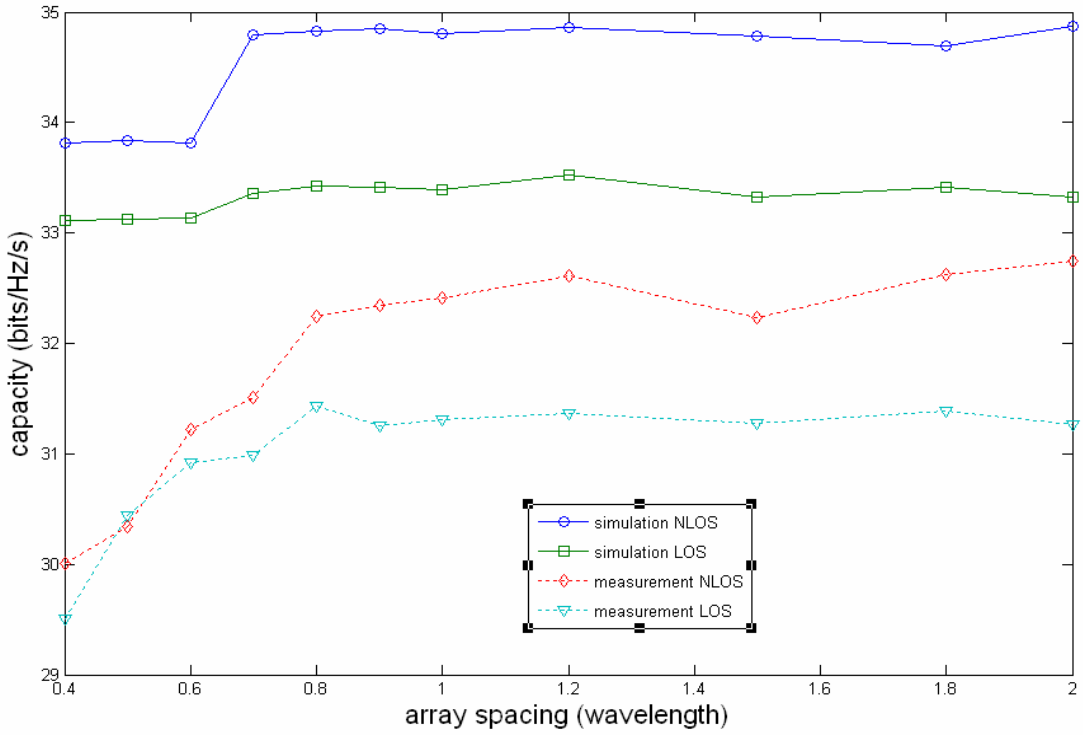

Fig. 5-3(b) Capacity versus array spacing simulation and measurement (PA no. 2) d=7m (NLOS, LOS)

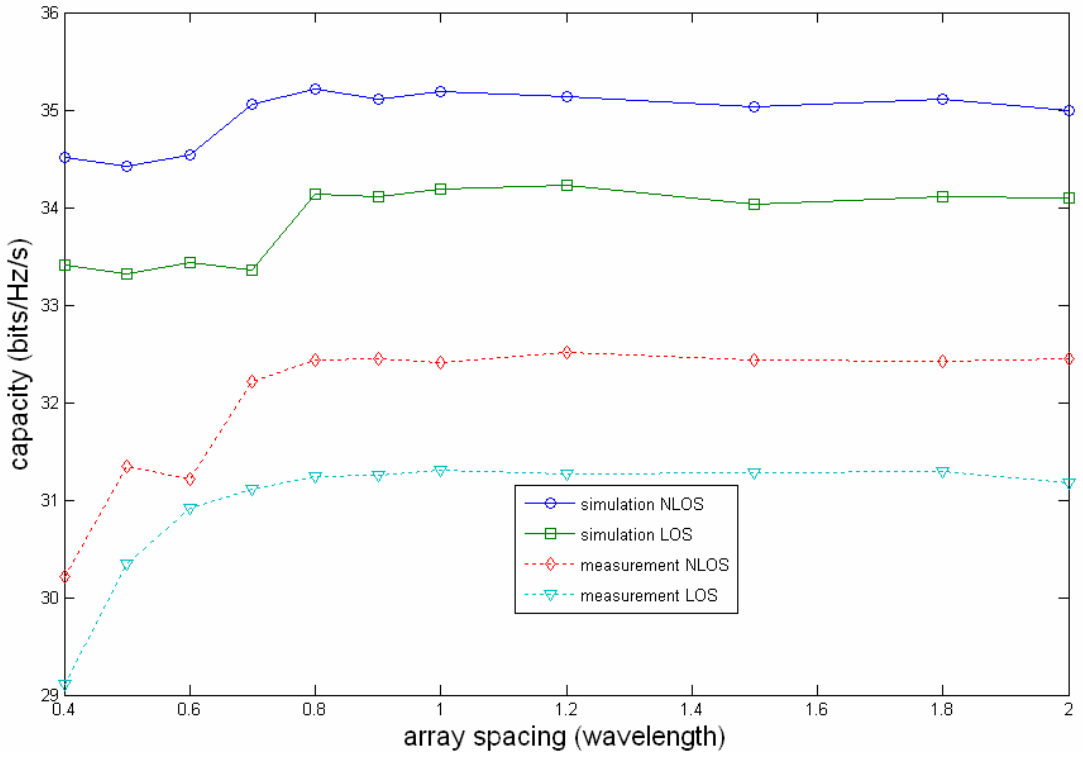

Fig 5-3 (c) Capacity versus array spacing simulation and measurement (PA no. 3) d=7m (NLOS, LOS)

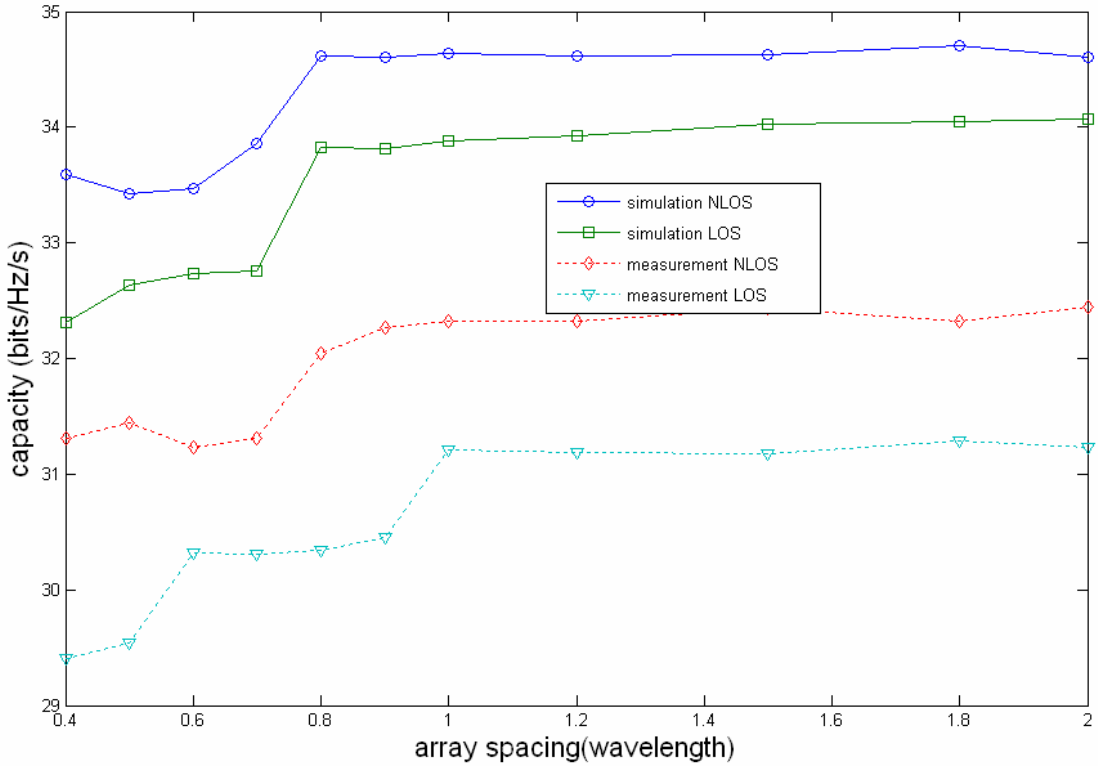

Fig. 5-3 (d) Capacity versus array spacing simulation and measurement (PA no. 4) d=7m (NLOS, LOS)

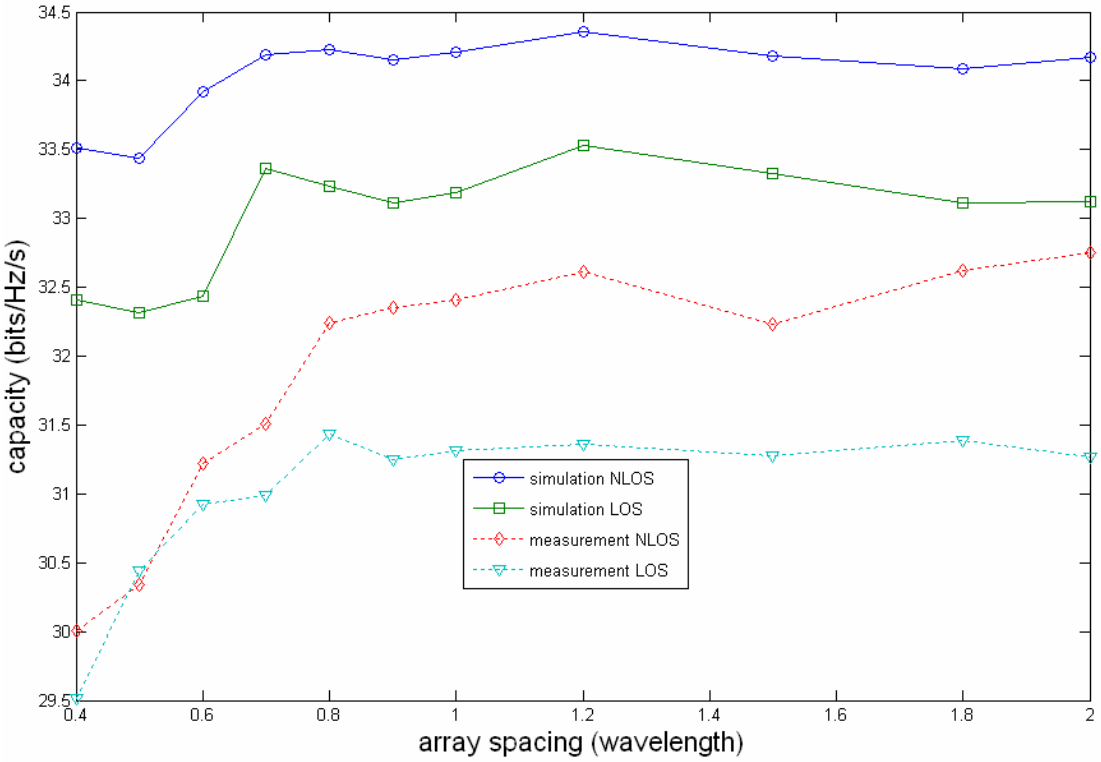

Fig. 5-3 (e) Capacity versus array spacing simulation and measurement (PA no. 5)

Distance=7m (NLOS, LOS)

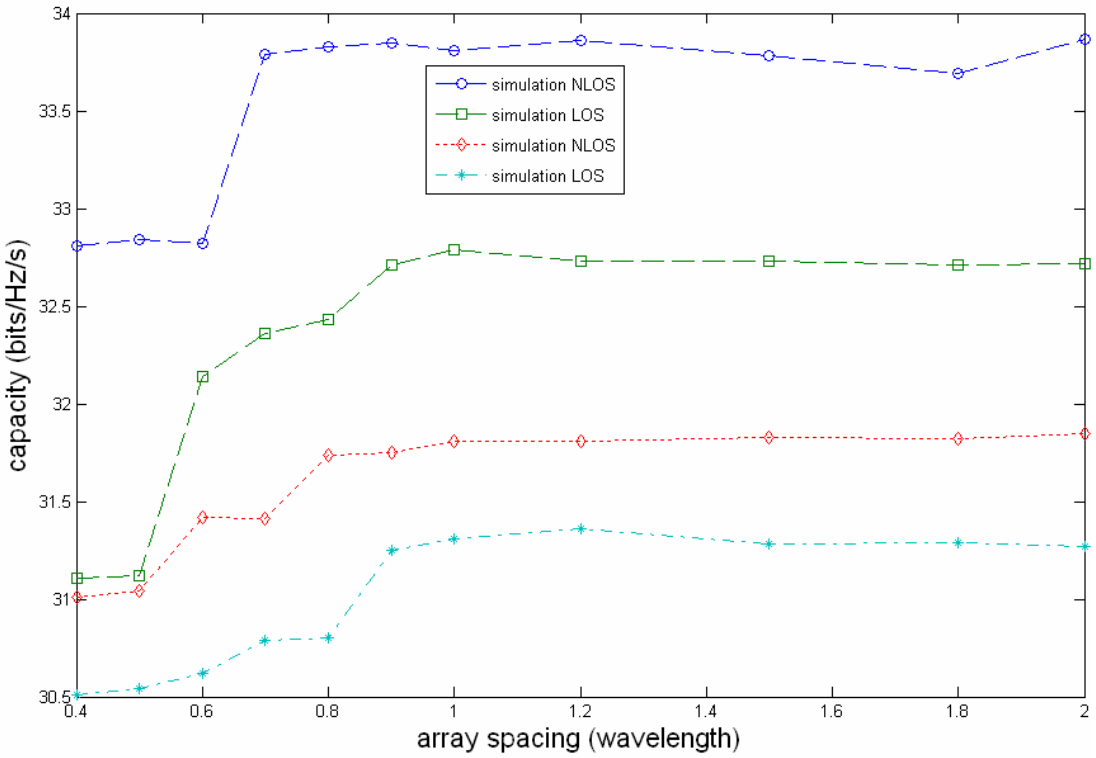

Fig. 5-3 (f) Capacity versus array spacing simulation and measurement (PA no. 6)

d=7m (NLOS, LOS)

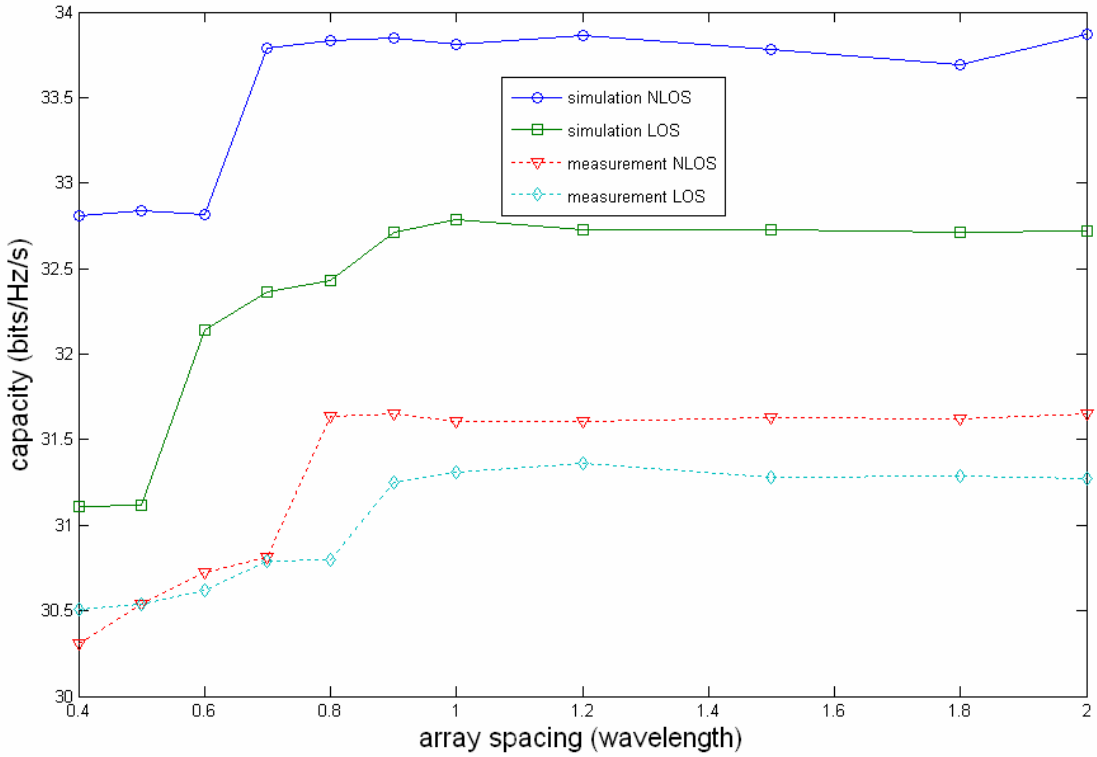

Fig. 5-3(g) Capacity versus array spacing simulation and measurement (PA no. 7) d=7m (NLOS, LOS)

Chapter 6

Conclusion

Effects of array spacing, array multi-polarization, number of array elements, frequency response, bandwidth, and propagation distance on M×N MIMO cahnnel capacity are explored by extended measurement in indoor environments. Six sites and seven polarization arrangements are considered for the measurement. We also have developed a geometrical–based scattering model for multi-polarized MIMO channels, which is validated by the measurement results.

Some phenomena are observed from the measurement results and are summarized as the following:

(1) It seems that the capacity increases as the elements spacing increases, which is due to the increase of de-correlation effect as the spacing increases. This incremental is also increases with the propagation distance or number of array element, which is also due to the increase of de-correlation effect. It is noted that this incremental saturates asymptotically when the array spacing is larger than 0.7 λ or 0.8 λ. It is found that the array spacing has not much effect on the capacity in LOS situation especially when the number of array element is small. However, when the number of array element is

large and the total array length is also large, the overall de-correlation effect due to array spacing is increased and the MIMO capacity is increased. The richness of multipath components in NLOS situations made all phenomena become more obvious. (2) It is found that polarization mismatch of array elements can increase the capacity. It is noted this effect may be enhanced by increasing the propagation distances. (3) It is found that mismatch polarization can decrease the saturation length to 0.7 or 0.8 wavelengths. (4) The measurement results show that MIMO capacity frequency response is distributed randomly and changes slightly with propagation range. (5) The local scatterers around Tx/Rx array enhance MIMO capacity.

Appendix

When characterizing the dual-polarized scattering matrix $\mathbf{\Gamma}_0$, the different scattering coefficients Γ_{vv} , Γ_{hh} , Γ_{hv} ,and Γ_{vh} are calculated using the Fresnel theory and the UTD. For both mechanisms, the scattering coefficient corresponding to a given pair ,(m,n), with m and n standing for h (horizontal) and/or v (vertical) can be written as

$$\Gamma_{mn} = Rx^{T}(m) \cdot \mathbf{S} \cdot Tx(m) \qquad \text{(A-1)}$$

where Rx(m) and Tx(m) are 3 × one-unit vectors (expressed in a classical Cartesian coordinate system), respectively, representing the Tx and Rx antenna polarizations, i.e.,m and n and , and S is the 3 × 3 dyadic complex coefficient modeling the scattering mechanism (the superscript ^{T} is for transposition).

For reflected contributions, **S** is written as **R** and is expressed as

$$R = R_h \mathbf{e}_{inc,\|} e_{ref,\|}^{T} + R e_{\perp|} e_{\perp|}^{T} \qquad \text{(A-2)}$$

$$R_h = \frac{\varepsilon_{r,eff}\cos\theta_{inc} - \sqrt{\varepsilon_{r,eff} - \sin^2\theta_{inc}}}{\varepsilon_{r,eff}\cos\theta_{inc} + \sqrt{\varepsilon_{r,eff} - \sin^2\theta_{inc}}} \qquad \text{(A-3)}$$

$$R_{sd} = \frac{\cos\theta_{inc} - \sqrt{\varepsilon_{r,eff} - \sin^2\theta_{inc}}}{\cos\theta_{inc} + \sqrt{\varepsilon_{r,eff} - \sin^2\theta_{inc}}} \qquad \text{(A-4)}$$

where, $\mathbf{e}_{inc,\parallel}$ $e_{ref,\parallel}^{T}$ and $e_{\perp|}$ and are unit vectors in the directions of the incident/reflected signals parallel and perpendicular to the plane of incidence, respectively. $\varepsilon_{r,eff}$ is the complex effective relative permittivity and θ_{iinc}^{d} is the incident angle [40]. Regarding diffraction, **S** is the UTD dyadic finite-conductive wedge-diffraction coefficient **D**, the expression of which can be found in [40].

Reference

[1] Svantesson, T.; Wallace, J.;Communications "On signal strength and multipath richness in multi-input multi-output systems " IEEE International Conference on Volume 4, 11-15 May 2003 Page(s):2683 - 2687 vol.4.

[2] D. S. Shiu, G. J. Foschini, M. J. Gans, and J. M. Kahn, "Fading correlation and its effect on the capacity of multielement antenna systems," *IEEE Trans. Commun.*, vol. 48, pp. 502–513, 2000.

[3] A. M. Sengupta and P. P. Mitra, "Capacity of Multivariate ChannelsWith Multiplicative Noise: I. Random Matrix Techniques and Large-N Expansions for Full Transfer Matrices," Bell Labs., 2000.

[4] A. L. Moustakas, H. U. Baranger, L. Balents, A. M. Sengupta, and S. H. Simon, "Communication through a diffusive medium: Coherence and capacity," *Science*, vol. 287, pp. 287–290, 2000.

[5] D. Chizhik, F. R. Farrokhi, J. Ling, and A. Lozano, "Effect of antenna separation on the capacity of BLAST in correlated channels," *IEEE Commun. Lett.*, vol. 4, pp. 337–339, 2000.

[6] D. Chizhik, G. J. Foschini, and R. A.Valenzuela, "Capacities of multi-element transmit and receive antennas: Correlations and keyholes," *Electron.*

Lett., vol. 36, pp. 1099–1100, 2000.

[7] A. Gorokhov, "Transmit diversity versus SDMA: Analytic and numerical comparisons," in *Proc. IEEE Int. Conf. Communications*, New Orleans, LA, 2000, pp. 1020–1024.

[8] K. I. Pedersen, J. B. Andersen, J. P. Kermoal, and P. Mogensen, "A stochastic multiple-input–multiple-output radio channel model for evaluation of space-time coding algorithms," in *Proc. IEEE Vehic. Technol. Conf.*, Boston, MA, 2000, pp. 893–897.

[9] P. F. Driessen and G. J. Foschini, "On the capacity formula for multiple input–multiple output wireless channels: A geometric interpretation," *IEEE Trans. Commun.*, vol. 47, pp. 173–176, 1999.

[10] C. N. Chuah, J. M. Kahn, and D. Tse, "Capacity of multi-antenna array systems in indoor wireless environment," in *Proc. IEEE Global*

[11] T. A. Chen, M. P. Fitz, W. Y. Kuo, M. D. Zoltowski, and J. H. Grimm, "A space-time model for frequency nonselective Rayleigh fading channels with applications to space-time modems," *IEEE J. Select. Areas Commun.*, vol. 18, pp. 1175–1190, 2000.

[12] A. F. Naguib, V. Tarokh, N. Seshadri, and A. R. Calderbank, "A space-time coding modem for high-data-rate wireless communications,"

IEEE J. Select. Areas Commun., vol. 16, pp. 1459–1478, 1998.

[13] J. H. Winters, “On the capacity of radio communication systems with diversity in a rayleigh fading environment,” *IEEE J. Select. Areas Commun.*, vol. 5, pp. 871–878, June 1987.

[14] Pohl, V.; Jungnickel, V.; Haustein, T.; von Helmolt, C., “Antenna Spacing in MIMO Indoor channels,” Vehicular Technology Conference, 2002. VTC Spring 2002, IEEE 55th, vol.2, pp. 749 –753, May 2002

[15] Jeng-Shiann Jiang; Ingram, M.A.; ”Enhancing measured MIMO capacity by adapting the locations of the antenna elements,” Personal, Indoor and Mobile Radio Communications, 2002. The 13th IEEE International Symposium on, vol.3, pp.1027 – 1031, Sept. 2002

[16] K. I. Pedersen and P. Mogensen, “Simulation of dual-polarized propagation environments for adaptive antennas,” in *Proc. IEEE VTC’99*, 1999, pp. 62–66.

[17] B. Lindmark and M. Nilsson, “On the available diversity gain from different dual-polarized antennas,” *IEEE J. Select. Areas Commun.*, vol. 19, pp. 287–294, Feb. 2001.

[18] R. G. Vaughan, “Polarization diversity in mobile communications,” *IEEE Trans. Veh. Technol.*, vol. 39, pp. 177–186, Aug. 1990.

[19] L. M. Correia, *COST 259—Wireless Flexible Personalised Communications*. Chichester, U.K.: Wiley, 2001.

[20] P. Soma, D. S. Baum, V. Erceg, R. Krishnamoorthy, and A. J. Paulraj,

"Analysis and modeling of multiple-input multiple-output radio channels based on outdoor measurements conducted at 2.5 GHz for fixed BWA applications," in *Proc. IEEE ICC'02*, New York, 2002.

[21] R. B. Ertel, P. Cardieri, K.W. Sowerby, T. S. Rappaport, and J. H. Reed, "Overview of spatial channel models for antenna array communication systems," *IEEE Pers. Commun.*, vol. 5, pp. 10–22, Jan. 1998.

[22] A. M. Saleh and R. A. Valenzuela, "A statistical model for indoor multipath propagation," *IEEE J. Select. Areas Commun.*, vol. SAC-5, pp. 128–137, Feb. 1987.

[23] J. C. Liberti and T. S. Rappaport, "A geometrically based model for line-of-sight multipath radio channels," in *Proc. IEEE VTC'96*, 1996, pp. 844–848.

[24] M. Lu, T. Lo, and J. Litva, "A physical spatio-temporal model of multipath propagation channels," in *Proc. IEEE VTC'97*, 1997, pp. 1810–1814.

[25] J. J. Blanz and P. Jung, "A flexibly configurable spatial model for mobile radio channels," *IEEE Trans. Comm.*, vol. 46, pp. 367–371, Mar. 1998.

654 IEEE TRANSACTIONS ON VEHICULAR TECHNOLOGY, VOL. 53, NO. 3, MAY 2004

[26] J. Fuhl, A. F. Molisch, and E. Bonek, "A unified channel model for mobile radio systems with smart antennas," *Proc. IEEE* , vol. 145, pp. 32–41, Jan. 1998.

[27] A. Abdi and M. Kaveh, "A space–time correlation model for multielement antenna systems in mobile fading channels," *IEEE J. Select. Areas*

[28] Palomar, D.P.; Fonollosa, J.R.; Lagunas, M.A.; "Capacity results of spatially correlated frequency-selective MIMO channels in UMTS "in proc. IEEE VTC' 01

vol.2 2001,pp 553-557

[29] L.H Brandenburg and A.D.Wyner, ",Capacity of Gaussian channel with memory:The multivariate case, " Bell syst.Tech.J.,vol 53,no.5 pp.745-778,1974.

[30] C. Oestges, "Astochastic geometrical vector model of macro- and megacellular communication channels," *IEEE Trans. Veh. Technol.*, vol. 51, pp. 1352–1360, Nov. 2002.

[31] M. Toeltsch, J. Laurila, K. Kalliola, A. F. Molisch, P. Vainikainen, and E. Bonek, "Statistical characterization of urban spatial radio channels," *IEEE J. Select. Areas Commun.*, vol. 20, pp. 539–549, Apr. 2002.

[32] R. G. Vaughan, "Polarization diversity in mobile communications," *IEEE Trans. Veh. Technol.*, vol. 39, pp. 177–186, Aug. 1990.

[33] T. B. Sørensen, A. Ø. Nielsen, P. E. Mogensen, M. Tolstrup, and K. Steffensen, "Performance of two-branch polarization antenna diversity in an

[34] P. Kyritsi, D. C. Cox, R. A. Valenzuela, and P. W. Wolniansky, "Effect of antenna polarization on the capacity of a multiple element system in an indoor environment," *IEEE J. Select. Areas Commun.*, vol. 20, pp. 1227–1239, Aug. 2002.